NASA Technical Memorandum 89125

A Study of High-Lift Airfoils at High Reynolds Numbers in the Langley Low-Turbulence Pressure Tunnel

Harry L. Morgan, Jr., James C. Ferris, and Robert J. McGhee

Langley Research Center
Hampton, Virginia

SUMMARY

An experimental study has been conducted in the Langley Low-Turbulence Pressure Tunnel to determine the effects of Reynolds number and Mach number on the two-dimensional aerodynamic performance of two supercritical-type airfoils, one equipped with a conventional flap system and the other with an advanced high-lift flap system. The conventional flap system consisted of a leading-edge slat and a double-slotted, trailing-edge flap with a small-chord vane and a large-chord aft flap. The advanced flap system consisted of a leading-edge slat and a double-slotted, trailing-edge flap with a large-chord vane and a small-chord aft flap. Both models were tested with all elements nested to form the cruise airfoil and with the leading-edge slat and the double-slotted, trailing-edge flap deflected to form the high-lift airfoils. Each high-lift airfoil was also tested with the double-slotted flaps nested to form a single-slotted, trailing-edge flap. The experimental tests were conducted through a Reynolds number range from 2.8 to 20.9 $\times$ 10^6 and a Mach number range from 0.10 to 0.35. Lift and pitching-moment data were obtained using the tunnel force-balance and model-support system. Each model was instrumented with a chordwise row of surface static pressure taps located at the midspan position. Limited drag data were obtained using the downstream wake-rake traversing system.

The test results demonstrate the tremendous effect of Reynolds number and Mach number on the lift performance of both high-lift airfoils. Analysis of the test data revealed several inconsistencies in the trends observed showing the effect of increased Reynolds number on lift performance. The results of gap and overlap optimization studies demonstrate the extreme sensitivity of the positioning of the leading-edge slat on maximum lift performance. The high-lift test techniques developed show that some form of tunnel sidewall boundary-layer control is absolutely necessary to ensure spanwise uniformity of the flow on the surface of a high-lift airfoil near conditions of maximum lift and stall. The limited drag data obtained show that the slat and flap support brackets on a high-lift airfoil have a detrimental effect on the spanwise uniformity of the downstream wake flow.

INTRODUCTION

The National Aeronautics and Space Administration has in recent years undertaken an extensive research effort aimed at improving the aerodynamic performance of a wide range of military, commercial, and general aviation aircraft. A large part of this research effort has been focused on improvements in the cruise performance of those aircraft by reducing the total aerodynamic drag and by increasing the drag-rise Mach number of the wing. Since the mid-1960's, several new families of airfoils have been developed with improved cruise performance characteristics; these include airfoils in the supercritical (SC), laminar-flow-control (LFC), general aviation (GA), and natural-laminar-flow (NLF) series. These new airfoils were designed using the latest theoretical design and analysis methods, and they have demonstrated greatly improved cruise performance characteristics compared with the earlier developed NACA airfoils designed primarily using trial-and-error experimental methods. In general, no matter how much effort is devoted to improving the cruise performance characteristics of an airfoil, the airfoil cannot be utilized unless it can be equipped with a flap system that will produce sufficient lift to meet takeoff and landing performance requirements without unreasonable increases in wing area. This fact is often overlooked by

the airfoil designer, and as a result many otherwise excellent airfoils are never put into practical use.

The performance of the airfoil high-lift system is a very important factor in the overall design of a new aircraft wing. Small improvements in the lift-drag ratio and maximum lift produced by the high-lift system often translate into large reductions in wing size and weight. The overall objective of the high-lift-system designer is to equip the wing with a flap system that has as few elements as possible to reduce mechanical complexity and weight, that produces the maximum possible lift to reduce landing speeds, and that produces a high lift-drag ratio to reduce fuel consumption during takeoff and climb. The viscous flow fields associated with high-lift systems are very complex, and only a few theoretical analysis codes exist that reliably predict the aerodynamic performance of these systems. Most of these codes are applicable only to two-dimensional analysis in fully attached flow conditions. Therefore, the design and analysis of high-lift systems currently rely heavily on the experience and judgment of the individual aerodynamicist. Total results of aerodynamic performance, especially maximum lift with its associated regions of highly separated flow, can be obtained only by expensive and time-consuming wind-tunnel tests or by actual flight test programs. Conversations with aircraft manufacturers have repeatedly revealed their inability to correlate wind-tunnel and free-flight test results for low-speed, takeoff and landing conditions. In several instances, major and very expensive high-lift-system design modifications were necessary because of poor flight performance. It is therefore very important that both theoretical and experimental research be conducted to study the effects of Reynolds number on high-lift-system performance.

A review of available research literature has shown that very little experimental data exist demonstrating the effect of Reynolds number on high-lift-system performance. Most low-speed wind tunnels are nonpressurized and capable of simulating only a fraction of the full-scale flight Reynolds number at the correct Mach number. There are, however, a small number of wind tunnels capable of obtaining full-scale conditions at the correct Mach number. One such tunnel is the Langley Low-Turbulence Pressure Tunnel (LTPT), which is a 10-atm pressurized facility with a 3- by 7.5-ft test section that is ideally suited for two-dimensional-airfoil testing at high Reynolds numbers and low speeds. The LTPT has recently been renovated to improve its high-lift testing capability and, as a result, is now a unique facility for high-lift-airfoil testing at high Reynolds numbers.

The purpose of this paper is to present a summary of the results of two high-lift-airfoil tests recently conducted in the LTPT. The primary objectives of these tests were to develop high-lift test techniques and to establish a high Reynolds number, high-lift data base for flight correlation and for verification with existing theoretical analysis methods. Summaries of test results for each airfoil with all elements nested (cruise configuration) and with the leading-edge slat and both single- and double-slotted, trailing-edge flaps deflected (high-lift configurations) will be presented, and comparisons between trends observed showing the effect of Reynolds number on lift performance of each airfoil will be discussed. The high-lift testing techniques developed during this investigation will also be discussed. The formation of ice on the leading edges of an aircraft wing and tail may cause a severe loss in the performance of the lifting surfaces, especially the horizontal tail surfaces that are often difficult to treat. To investigate the effects of Reynolds number on lift loss due to frost and glaze ice, tests were conducted on one of the cruise airfoils with leading-edge modifications to simulate both frost and extensive glaze ice buildup. These test results will also be presented and discussed.

2

All measurements and calculations were made in the U.S. Customary Units.

C_p local static pressure coefficient

c airfoil reference chord, in.

c_d section drag coefficient

c_l section lift coefficient

c_m section pitching-moment coefficient

M_∞ free-stream Mach number

$\dot{m}$ mass-flow rate, slugs/min

$p_{t,\infty}$ tunnel free-stream total pressure, lb/ft^2

R_c Reynolds number based on airfoil reference chord

x/c nondimensional distance x measured along chord of flap c

α angle of attack, deg

δ slat or flap deflection (positive for trailing edge down), deg

Subscripts:

f   flap

max   maximum

s   slat

v   vane

vf   vane/flap combination

$\alpha=0$ angle of attack of 0°

Abbreviations:

AOA   angle of attack

BLC   boundary-layer control

LE   leading edge

LTPT   Low-Turbulence Pressure Tunnel

TE   trailing edge

2-D   two-dimensional

WIND-TUNNEL FACILITY AND TEST APPARATUS

Tunnel

The high-lift-airfoil tests were conducted in the Langley Low-Turbulence Pressure Tunnel (LTPT). The LTPT is a single-return, closed-throat wind tunnel that can be operated at tunnel total pressures from near-vacuum to 10 atm (ref. 1). A sketch of the tunnel circuit arrangement is shown in figure 1. The tunnel test section is 3 ft wide, 7.5 ft high, and 7.5 ft long, which when combined with a 17.6-to-1 contraction ratio makes the LTPT ideally suited for two-dimensional airfoil testing. The Reynolds number capability of the tunnel for a typical high-lift-airfoil test is shown in figure 2. The tunnel can obtain a maximum Reynolds number of 15×10^6 per foot at a Mach number of 0.24. The maximum empty-tunnel speed at a total pressure of 1 atm is a Mach number of 0.47 with a corresponding Reynolds number of 3×10^6 per foot.

Model-Support and Force-Balance System

A major part of the recent tunnel renovation was the installation of a new model-support and force-balance system capable of handling both single- and multi-element airfoils for high Reynolds number testing. A sketch of this new model-support and force-balance system is shown in figure 3. The airfoil model is mounted between two end plates that are connected to the inner drums. These inner drums are held in place by an outer drum and yoke arm support system. The yoke arm support system is mounted to the force balance, which is connected to the tunnel through a balance platform. The attitude of the model is controlled by a motor-driven, externally mounted pitch mechanism that rotates the bearing-mounted inner drums. A multipath labyrinth seal is used to minimize air leakage from the test section into the outer tunnel plenum.

The force balance is a three-component strain-gauge balance of the external virtual-image type. The maximum balance loads are 18 000 lb in lift, 550 lb in drag, and 12 000 ft-lb in pitching moment. The balance is temperature compensated and calibrated to account for first- and second-order interactions, and it has a general accuracy of ±0.5 percent of design loads.

Sidewall Boundary-Layer Control System

To ensure spanwise uniformity of the flow field when testing high-lift airfoils near the maximum lift condition, some form of tunnel sidewall boundary-layer control (BLC) is needed. The large adverse pressure gradients induced on the tunnel side-walls by a high-lift airfoil near maximum lift can cause the sidewall boundary layer to separate with a corresponding loss of spanwise uniformity of the flow on the airfoil surface and a resulting loss of lift. Because a source of high-pressure air was available for the LTPT, tangential blowing was selected as the means of providing sidewall BLC. Five blowing boxes with tangential blowing slots are available for each side of the tunnel and can be positioned around the airfoil within the confines of the airfoil end plates. High-pressure air is supplied to each box through a flexible hose connected to a blowing-box control cart with remote-controlled valves for each box. A cross-section sketch of a typical blowing box is presented in figure 4. The blowing boxes were designed to provide uniform tangential flow at the slot exit. Air enters an inner manifold distribution chamber and is distributed

through slots to an outer manifold chamber. The exit slot is formed by a removable slot lip and the box itself. The width of the slot exit may be varied to control the maximum mass-flow rate through the box.

During the tests of the second high-lift airfoil, a 0.25-in-diameter blowing tube located at the juncture between the airfoil and the end plate was used at two chordwise positions instead of the normal blowing box. An additional form of side-wall BLC is also available as an upstream floor-to-ceiling suction slot located on each sidewall. This slot is located approximately 20 in. upstream of the forward edge of the end plate. The boundary layer ingested through these slots by large suction pumps located under the floor of the test section is dumped into the down-stream diffuser. These suction pumps have limited power and are operational only at tunnel total pressures below 2 atm.

Remote-Controlled Wake Survey Apparatus

The airfoil drag data were determined during this investigation by the momentum method using measured downstream wake properties rather than by trying to correct the force-balance reading for end plate skin-friction drag and blowing-box air line tares. A remote-controlled survey arm was used to traverse the rake probe head through the airfoil wake. A sketch of this apparatus is presented in figure 5. The arm is composed of three movable components: a main boom, an offset boom, and a forward-pivoting rake head. Each component has a position control device. The main boom is mounted on the strut with a pivot point allowing rotation in the vertical plane. Its motion is controlled by the linear actuator. The offset boom can be rotated about the main boom by the roll actuator, which allows survey positions to be made at distances up to 12 in. from the tunnel centerline. The forward-pivoting rake head is mounted at the end of the offset boom and may be rotated in the vertical plane by the internally mounted pitch-adjustment mechanism. The position and rate of movement of the survey apparatus are controlled by a microprocessor controller.

A sketch showing the details of the wake survey rake is presented in figure 6. The rake is composed of two flow-angularity probes, seven total pressure probes, and four static pressure probes. Two types of static pressure probes were used, the standard type and the disk type. The standard-type probe consists of a 0.125-in-diameter tube with a hemispherical head. Each static pressure tube has eight flush orifices drilled 45° apart and located eight tube diameters from the tip of the tube. The disk probe is 0.437 in. in diameter and had a 0.18-in-diameter hole drilled through the center with an internal passage connecting this hole to the edge of the disk. The flow-angularity probes are located at the ends of the rake and are used to align the rake with the airfoil wake.

DESCRIPTION OF HIGH-LIFT AIRFOIL MODELS

Two high-lift models were tested during this investigation. Both models are supercritical-type airfoils equipped with a leading-edge slat and single- and double-slotted, trailing-edge flaps. A sketch of the model geometry and blowing-box loca-tions for each model is presented in figure 7. The most notable difference between the two models is the relative sizes of the trailing-edge vane/aft-flap combinations. The first model tested has a double-slotted flap composed of an advanced large-chord vane and small-chord aft flap (ref. 2), and the second model has a more conventional small-chord vane and large-chord aft flap (ref. 3). Because of this fundamental

geometric difference, the first model is referred to as the "large-vane model" and the second as the "small-vane model." Both models were also configured and tested with a single-slotted, trailing-edge flap and with all elements nested to form the cruise configuration.

The large-vane model has a cruise airfoil chord of 22 in. and a maximum thickness-chord ratio of 11.55 percent. The leading-edge slat, trailing-edge vane, and aft-flap elements have respective chords of 14.48, 20.93, and 14.03 percent of the cruise chord. The main element with slat and flaps deflected has a chord of 83.03 percent of the cruise chord. The single-slotted, trailing-edge flap has a 30 percent chord. This model was tested in the cruise configuration and in the single- and double-slotted flap configurations, and it was also equipped with a small 3-percent-chord 30° wedge attached to the lower surface trailing edge of the most downstream element. This wedge was used to simulate the split flap commonly referred to as a "Gurney flap." The high-lift configuration with slat and double-slotted flap deflected is instrumented with 142 centerline chordwise surface pressure taps and five spanwise rows of 10 taps each. The spanwise rows consist of one row near the trailing edge of the slat, main, vane, and aft-flap elements and one additional row midchord on the vane. Photographs of the large-vane model mounted in the LTPT are presented in figures 8 and 9. As shown in figure 9 the model is equipped with four chordwise rows of slat and flap support brackets symmetrically located 3.85 and 13.25 in. from the end plate. The brackets nearest the end plates are thicker to accommodate the pressure tap tubing carried over from the slat and flaps to the internal routing cavity in the main element.

The small-vane model has a cruise airfoil chord of 24 in. and a maximum thickness-chord ratio of 11 percent. The main, vane, and aft-flap elements have chords of 74.2, 6.43, and 24.4 percent of the cruise airfoil chord, respectively. The single-slotted, trailing-edge flap has a chord of 28.1 percent. The model can be configured with three different slats, as illustrated in figure 10. The baseline slat has a chord of 13 percent with the same leading-edge shape as that of the cruise airfoil. The large-chord slat has a chord of 19.5 percent with the same leading-edge shape as the baseline slat. The large-radius slat has a chord of 13 percent with a modified leading-edge shape and has a larger radius than the baseline slat with several degrees of droop. During the tests of the large-chord and large-radius slats, the leading edge of the main element was not modified to accommodate the slat shapes properly in the nested condition. During the tests of the small-vane, double-slotted flap configurations, the aft flap was moved downstream of the vane in the flaps-up configuration and then both elements were deflected to the same deflection angle. The small-vane, high-lift configuration is instrumented with 74 centerline chordwise surface pressure taps and 2 additional chordwise rows of 10 sparsely spaced taps located 6 in. from each end plate. The model also has 1 spanwise row of 8 taps near the trailing edge of the main element and a spanwise row of 10 taps along the trailing edge of the aft flap. This model is also equipped with four chordwise rows of slat and flap brackets symmetrically located at the juncture of the model with the end plate and 12 in. from the end plate, as shown in figure 11.

The BLC blowing boxes on the end plates for each model are positioned to energize the sidewall boundary layer near the regions of maximum velocity of the flow around the high-lift airfoil. These regions are typically those near the leading edge of each element and near the trailing edge of the main element. Each end plate for the large-vane model is instrumented with five blowing boxes, as illustrated in figure 7(a). Each end plate for the small-vane model is instrumented with three blowing boxes and two 0.25-in-diameter blowing tubes, as illustrated in figure 7(b).

The leading-edge blowing tube on this model is located near the leading edge of the main element and blows tangentially into the juncture between the model upper surface and the end plate, as shown in figure 12. The trailing-edge blowing tube is located in the cove region of the main element and blows tangentially around the juncture of the vane and the end plate, as shown in figure 13.

The small-vane cruise configuration was also tested with simulated leading-edge frost and glaze ice buildup. Partial frost conditions were simulated with 0.5-in-wide strips of No. 70 grit located on the upper and lower surfaces at a distance of approximately 3 percent of the chord from the leading edge. Full frost conditions were then simulated by filling the leading-edge space between the two partial frost strips with No. 70 grit. The glaze ice buildup was simulated by attaching a wooden piece to the leading edge of the airfoil with a shape approximating that of an actual buildup (ref. 4). A sketch showing the comparison between the simulated condition and an actual measured glaze ice shape is presented in figure 14. The simulated glaze ice shape was further enhanced by coating the wooden piece with an extremely coarse grit, as shown in the photograph presented in figure 15.

During the tests of the large- and small-vane, high-lift configurations, the gaps and overlaps of the slat and flap elements were varied to determine their effect on lift performance. A sketch illustrating the definition of gap and overlap is presented in figure 16. The gap is defined as the shortest distance between the lower surface trailing-edge point of the forward element and the upper surface of the aft element. The overlap is defined as the distance parallel to the airfoil reference chord line between the trailing-edge point of the forward element and the perpendicular projection of the most forward leading-edge point of the aft element.

TEST CONDITIONS

Both the large- and small-vane models were tested in the LTPT through an angle-of-attack range from -4° to several degrees past the maximum lift or stall condition, through a Mach number range from 0.10 to 0.35, and through a Reynolds number range from 2.8 to 20.9 × 10^6. Corrections for solid and wake blockage were applied to the free-stream dynamic pressure, and corrections for the effects of floor and ceiling constraint on streamline curvature were applied to lift, pitching moment, and angle of attack (ref. 5). The airfoil lift and pitching-moment coefficients were determined by measurements made with the force balance and by machine integration of the measured surface static pressures. A typical comparison between the force balance and machine-integrated lift and pitching-moment coefficients for the small-vane, high-lift model is presented in figure 17. As shown in this figure, the overall agreement in lift coefficients was generally very good considering the sparse number of surface pressure taps on the vane and flap elements. The agreement in pitching-moment coefficients was generally not as favorable as that for the lift coefficients because of the numerical sensitivity of the axial component of the pressure forces on the integration. A small error in the axial component of the pressure force (thrust force) results in a relatively large error in the integration of the pitching-moment coefficient.

Limited drag data were obtained from integration of the measured static and total pressures in the wake (ref. 6). The drag measurement technique used produced excellent results for the large-vane cruise configuration; however, the slat and flap support brackets of the high-lift configuration had a detrimental effect on the drag measurement. A partial spanwise variation of the drag coefficient for the large-vane,

high-lift configuration is shown in figure 18. The drag values presented in this figure were measured at a distance of approximately 1 chord length downstream of the trailing edge of the main element.

The presence of the support brackets causes a local deficit in the flow through the slot immediately downstream of the bracket which, in turn, causes a local thickening of the boundary layer. This thickened boundary layer feeds downstream into the wake as a large deficit and resultant high drag. Vortices are also generated at the juncture between the brackets and element surfaces, thus causing a spreading of the wake thickening due to the brackets. This spreading effect is indicated in figure 18 by the increase in drag on both sides of the bracket centerline. The current highly cantilevered, slow-moving, wake-rake traverse system is designed for application to cruise airfoils with relatively thin, symmetric wakes. In contrast, the high-lift configurations tested had very thick, multilayered, and highly turbulent wakes that cause considerable vibration and stress on the traverse system and take considerable tunnel time to measure. Because of the bracket and vibration problems encountered, all drag measurements with the existing traverse system were discontinued after the initial tests of the large-vane model.

The support brackets not only have a detrimental effect on drag but also, under certain conditions, on the lift as illustrated in figure 19 for the small-vane, high-lift configuration at low Reynolds number. The data in this figure show the favorable effect of removing the two inner leading-edge slat brackets. The brackets probably have a less detrimental effect on both lift and drag at the high Reynolds number test conditions because of thinning of the boundary layers that develop on the airfoil and bracket surfaces. During high Reynolds number testing in a pressurized facility like the LTPT, it is not generally feasible to eliminate high-lift support brackets entirely and rely solely on end plate support because of the high loads generated. One possible solution to the bracket problem is to blow high-pressure air immediately behind the support brackets in order to reduce their deficit effect on the slot flow.

HIGH-LIFT TEST PROCEDURES

During the tests of each cruise and high-lift configuration, the spanwise rows of surface pressures were monitored to check for spanwise uniformity of flow across the model. Fluorescent minitufts were also attached to the upper airfoil and end plate surfaces and were monitored via a video camera and ultraviolet light system to provide an additional check of the spanwise uniformity of the flow (ref. 7). The minituft pattern used during the tests of the large-vane model is partially visible in figure 8(b). Prior to the tests of each airfoil configuration, the mass-flow rates of the sidewall blowing boxes were adjusted to obtain spanwise uniformity of the flow across the airfoil at the condition of maximum possible lift. Once these mass-flow rates and their corresponding box-pressure ratios (the ratio of total pressure in the box to free-stream static pressure) were established, the mass-flow rates at other Reynolds number conditions were obtained by simply maintaining the same pressure ratios. Each blowing box had a remote-controlled pressure regulator that allowed for individual adjustment to account for asymmetries in slot openings between corresponding boxes on opposite end plates.

The basic procedure followed to determine the needed box-pressure ratios was first to bring the tunnel conditions up to the desired Mach number and Reynolds number and, with the pressure in all boxes off, increase the angle of attack of the

model to the stall condition where the surface tufts indicated a loss of spanwise uniformity of the flow on the model. The box pressures were then increased by starting with the most upstream box near the leading edge of the airfoil and then proceeding in an alternating right-to-left end plate manner downstream until spanwise uniformity of the flow was established. During the adjustment process, the airfoil and end plate flow patterns were constantly monitored using either the ultraviolet mini-tufts or, in some cases, conventional yarn tufts and the computer-plotted spanwise distribution of surface static pressures. The model angle of attack was then increased again until a loss of spanwise uniformity of the flow occurred; at that time, the box-pressure adjustment procedure was repeated with care shown to prevent overblowing. Overblowing would generate supercirculation near the juncture of the airfoil with the end plate and thus cause an increase in the spanwise loading at the juncture with a corresponding unrealistic maximum lift coefficient. The box-pressure adjustment procedure was repeated until the maximum possible lift coefficient had been obtained.

The box-pressure adjustment procedure worked very well for the small-vane, high-lift model; unfortunately, it was only marginally successful for the large-vane, high-lift model which was the first model tested. Previous tests of an NACA 4416 airfoil (ref. 1) equipped with a single-slotted flap showed that box slot openings of 0.030 in. were adequate; therefore, the same slot openings were used for the large-vane model. The maximum lift coefficient as a function of total box mass-flow rate for the large-vane, high-lift model is presented in figure 20 and shows that the maximum lift was just beginning to level off at the maximum obtainable mass-flow rate of 6 slugs/min, which corresponded to the condition of fully choked flow in each box. The total mass-flow rate could have been increased by increasing the slot openings but, as illustrated in figure 4, this would have required a complete removal of the end plates for additional machining which was not permissible during the allotted test period.

In an attempt to provide additional sidewall BLC during the tests of the large-vane model, the upstream floor-to-ceiling sidewall suction slots were utilized. The boundary layer ingested through these slots by large suction pumps located under the floor of the test section is dumped into the downstream diffuser. These suction pumps have limited power and are operational only at tunnel total pressures below 2 atm. A comparison of the lift performance of the large-vane cruise airfoil with suction on and off in which all blowing boxes operated at maximum mass-flow rate is presented in figure 21 and shows, instead of the expected improvement in lift performance, a loss in performance with the sidewall suction on. One possible explanation for this unexpected trend is that the noise level in the tunnel with suction on was greatly increased because of the sharpness of the suction slot lip. The increased noise level probably increased the free-stream turbulence level which, in turn, adversely affected the transition and separation characteristics of the boundary layers on the airfoil elements. Therefore, it was decided to discontinue the use of the sidewall BLC suction system and to continue the tests of the large-vane model operating the blowing boxes at maximum mass-flow rate. Because of the lack of adequate sidewall BLC control, the data obtained during the tests of the large-vane model are not representative of the maximum lift performance possible but they do show several very interesting trends with increased Mach number and Reynolds number.

During the tests of the small-vane, high-lift model, the blowing-box slot openings were set to 0.050 in. and leading- and trailing-edge blowing tubes were added to the main element. These two changes provided sufficient mass flow to prevent sidewall boundary-layer separation. The effect of the blowing box and tube

mass-flow rates on the lift coefficient obtained for the small-vane, high-lift model is presented in figure 22. As shown in this figure, the rather small leading-edge blowing tube, which blows high-energy air into the juncture between the airfoil and end plate downstream of the leading-edge pressure peak on the main element, had a considerable effect on the lift performance in view of the fact that it accounted for only approximately 5 percent of the total BLC mass-flow rate required to prevent sidewall separation. Unlike the large-vane model, the outer slat and flap support brackets for the small-vane model were located at the juncture between the model and end plate. The wall boundary layer at the model juncture is relatively thick compared with that on the model; therefore, support brackets located at the juncture would probably have a less detrimental effect on the ability of the end plate BLC system to maintain the spanwise uniformity of the flow. As previously discussed for the large-vane model, the inner support brackets probably have a detrimental effect on the lift performance of the small-vane model at low Reynolds numbers. In general, however, the data obtained for the small-vane, high-lift model are of excellent quality and show several very interesting trends with increased Mach number and Reynolds number.

DISCUSSION OF TEST RESULTS

The stall characteristics of an airfoil can generally be classified as either a leading-edge laminar boundary-layer separation or a trailing-edge turbulent boundary-layer separation. Leading-edge laminar-stall airfoils have linear lift versus angle-of-attack behavior below the angle of maximum lift or stall. Increasing the angle of attack past stall causes massive separation of the upper surface leading-edge laminar boundary layer with a resultant sharp drop in the lift. Trailing-edge turbulent-stall airfoils, on the other hand, have nonlinear lift versus angle-of-attack behavior below the stall angle because of the forward movement of the separation point of the turbulent boundary layer with increased angle of attack. Increasing the angle of attack past stall results in the continued forward movement of the trailing-edge turbulent separation point until the angle is reached where the leading-edge laminar boundary layer completely separates causing massive separation. Deflecting the trailing-edge flap elements of a trailing-edge turbulent-stall airfoil often causes the upper surface turbulent boundary layer on the main element to remain attached and, therefore, the flapped airfoil to exhibit leading-edge laminar-stall behavior provided the turbulent boundary layer on the upper surface of the flap remains attached. Even if the upper surface turbulent boundary layer on the flap separates, the separation point may remain stationary with increased angle of attack and the airfoil still exhibit laminar-stall behavior. It is important to keep in mind these two types of stall behavior during the discussion of the test results. Also during the discussion of the test results, the term "optimum" refers to the condition corresponding to the greatest obtained maximum lift coefficient.

Large- and Small-Vane Cruise Configurations

The effects of Reynolds number on the lift performance of the large- and small-vane cruise airfoils (slat and flap elements nested) are presented in figures 23 and 24, respectively. The data presented in figure 23 for the large-vane cruise airfoil show the trend of an increase in maximum lift coefficient and stall angle with increased Reynolds number. The maximum lift coefficient increased rapidly in the Reynolds number range from 3 to 5×10^6 and gradually in the range from 5 to 18×10^6. The lift coefficient versus angle-of-attack curves shown in figure 23(a) are nonlinear

10

below the stall angle. These trends are typical of an airfoil with a large leading-edge radius, such as this model and the NASA GA(W)-1 airfoil (ref. 8), which have reduced leading-edge pressure gradients and exhibit trailing-edge stall behavior. The data in figure 24 for the small-vane cruise airfoil show the trend of a gradual increase in maximum lift coefficient in the Reynolds number range from 3 to 7×10^6 followed by a decrease in maximum lift coefficient in the Reynolds number range from 7 to 12×10^6. A similar trend is evident from previous test data taken in the LTPT of an NACA 65_1-213 airfoil (ref. 9), which has a sharp leading-edge shape similar to that of the small-vane cruise airfoil. The curves for lift coefficient versus angle of attack shown in figure 24(a) are linear below the stall angle, which is also typical behavior for leading-edge laminar-stall airfoils. As illustrated in figure 25, the small-vane cruise airfoil has a smaller leading-edge radius than the large-vane airfoil and, therefore, should produce higher leading-edge pressure gradients and be more likely to exhibit leading-edge laminar-stall behavior.

The effect of Mach number on the lift performance of the large-vane cruise airfoil is presented in figure 26. The maximum lift coefficient data presented in figure 26(b) show that an increase in Mach number resulted in a very rapid decrease in the maximum lift coefficient at a Reynolds number of 3×10^6 and a more gradual decrease at 18×10^6. The separation of the leading-edge laminar boundary layer is strongly influenced by the local Mach number, pressure gradient, and boundary-layer thickness at the start of the laminar separation bubble. At a constant Mach number, the laminar boundary-layer thickness will decrease with increased Reynolds number and detach at higher angles of attack with resultant higher maximum lift coefficients. At a constant Reynolds number, the leading-edge-suction pressure peak will increase with increased Mach number, thus causing the laminar boundary layer to detach at lower angles of attack with resultant lower maximum lift coefficients. This is known as the "compressibility effect" as described in reference 10. The data presented in figure 26(a) also show that an increase in Mach number at a constant Reynolds number of 3×10^6 caused an increase in the lift coefficient at a given angle of attack and a large decrease in the stall angle.

The effect of the TE wedge on the lift performance of the large-vane cruise airfoil is presented in figure 27. As shown in figure 27(b), the small 3-percent-chord TE wedge attached to the lower surface trailing edge of the airfoil produced an approximate constant increase in maximum lift coefficient of 0.25 through the Reynolds number range from 8 to 18×10^6. The lift coefficient data presented in figure 27(a) show a decrease in the stall angle of attack of approximately 2° with the wedge on. These small wedges simulate a split flap and are very useful devices for tailoring the lift distribution across the span of a wing or horizontal tail surface. However, one disadvantage of the TE wedge is that a large trailing-edge separation region forms because of the bluntness of the wedge, which in turn produces greater drag than that which could be obtained by modifying the trailing-edge camber distribution to generate the same desired lift and pitching-moment characteristics.

Small-Vane Cruise Configuration With Slat Deflected

The effects of Reynolds number on the lift performance of the small-vane cruise configuration with the baseline slat deflected (typical climb configuration) are presented in figure 28. The maximum lift coefficient data presented in figure 28(b) show an increase in maximum lift coefficient of approximately 1.0 compared with that of the cruise configuration shown in figure 24(b). Deflecting the slat increases the leading-edge camber of the cruise airfoil to produce a large positive lift increment.

Moving the slat forward forms a slot that allows for the injection of high-energy air into the upper surface turbulent boundary layer on the main element to thin it and delay downstream separation and thus increases lift further. Unlike the cruise configuration, the climb configuration shows a continuous gradual increase in maximum lift coefficient with an increase in Reynolds number. This trend can be attributed to the fact that the deflection of the slat creates an equivalent airfoil with a larger effective leading-edge radius that will behave more like a trailing-edge than like a leading-edge stall airfoil.

Large- and Small-Vane Configurations With Slat and Single-Slotted Flap

The effect of flap deflection and TE wedge on the lift performance of the large-vane model equipped with the leading-edge slat and single-slotted trailing-edge flap are presented in figure 29. The maximum lift coefficient data presented in figure 29(b) show that the maximum lift coefficient increased with an increase in flap deflection from 15° (takeoff setting) to 30° (landing setting) followed by a decrease in the maximum lift coefficient to 35° (landing setting). The decrease in maximum lift coefficient can be attributed to an increase in the amount of separated flow on the flap element as indicated by the surface static pressure distributions as shown in figure 30. The data presented in figure 29(a) show that an increase in Reynolds number from 5 to 9 × 10^6 resulted in only a slight improvement in the maximum lift coefficient. These data also show the effect of the TE wedge on lift performance. The TE wedge produced a positive increment in lift coefficient of approximately 0.4 at the lower angles of attack that gradually decreased to approximately 0.2 at the stall angle of attack.

The effects of Reynolds number and flap deflection on the lift performance of the small-vane model equipped with the baseline leading-edge slat and single-slotted, trailing-edge flap are presented in figure 31. The data show that the maximum lift coefficient increased slightly with an increase in Reynolds number from 2.8 to 12 × 10^6 and that the flap deflection was 40° for the maximum lift coefficient obtained at both Reynolds numbers. As shown in figure 31(a), Reynolds number had little effect on lift performance except near the stall condition. The effects of Reynolds numbers on the optimization of the flap gap and overlap positions are presented in figure 32. These data show that at a constant overlap setting of 0-percent chord and a flap deflection of 40°, the maximum lift coefficient remained constant for gaps greater than 1-percent chord at a Reynolds number of 2.8 × 10^6 and that the maximum lift coefficient was just beginning to level off at the largest gap setting of 3-percent chord at a Reynolds number of 12 × 10^6. At a constant gap setting of 1-percent chord and a flap deflection of 37.5°, the maximum lift coefficient decreased with increasing overlap at a Reynolds number of 2.8 × 10^6, but it was optimum at the 0-percent overlap setting at a Reynolds number of 12 × 10^6. Although the gap and overlap optimizations were performed at different flap deflections, it is doubtful that the small difference in deflection had much effect on the results obtained.

Large-Vane Configuration With Slat and Double-Slotted Flap

The effects of sidewall BLC and leading-edge slat deflection on the lift performance of the large-vane, high-lift configuration with the slat and double-slotted flap are presented in figure 33. As shown in figure 33(a), sidewall BLC produced an increment in lift coefficient of approximately 0.5 through the entire angle-of-attack range and an approximate 3° decrease in the stall angle. As shown in figure 33(b),

the highest maximum lift coefficient obtained occurred at a slat deflection of -35°. The lift coefficient at an angle of attack of 0° changed only slightly with slat deflection, which indicates that the increase in maximum lift coefficient was possibly due primarily to the favorable effect of slat position on the separation of the flow on the flap.

The effects of Reynolds number on the lift performance of a large-vane, high-lift configuration with the slat deflected -35° and -30° are presented in figures 34 and 35, respectively. The effect of Reynolds number on the pitching-moment coefficients for these two slat deflections is presented in figure 36. A comparison of the data presented in figures 34 and 35 illustrates the difficulty of predicting the effects of Reynolds number on the performance of high-lift systems with leading-edge devices.

As shown in figure 34 with the TE wedge off, an increase in Reynolds number resulted in the expected increase in maximum lift coefficient with little change in the lift coefficient at an angle of attack of 0°. It is expected that an increase in Reynolds number will cause the boundary layers on all elements of a high-lift system to become thinner, thereby increasing the effective camber of each element with a resultant increase in circulation (total lift) and negative pitching moment. Furthermore, this boundary-layer thinning effect will be more pronounced for the trailing-edge flap elements that have larger chords and thicker boundary layers than the leading-edge slat element. The trend of greater thinning of the flap boundary layers with increased Reynolds number is evident from an examination of the pitching-moment coefficient data presented in figure 36 for a slat deflection of -35°. The pitching-moment coefficient became more negative with increased Reynolds number and angle of attack, thus indicating that the flap loading increased more than the slat loading.

The lift performance data presented in figure 35 for a slat deflection of -30° show, however, that the deflection of the slat has a much stronger influence on trailing-edge flap performance than would generally be expected. As shown in figure 35(b), an increase in Reynolds number caused the maximum lift coefficient and lift coefficient at an angle of attack of 0° to decrease, a result opposite to the trend observed for a slat deflection of -35°. As shown in figure 36, the reduction in the negative pitching-moment coefficient at this slat deflection indicates that the slat loading increased with increased Reynolds number without a corresponding increase in flap loading.

The effect of the TE wedge on the lift performance of the large-vane, double-slotted flap configuration is presented in figure 34(b). The TE wedge increased the maximum lift coefficient by approximately 0.1 at a Reynolds number of 3×10^6, decreased it by 0.1 at a Reynolds number of 9×10^6, and had no effect at a Reynolds number of 16×10^6. The TE wedge had little effect on the variation of the lift coefficient at an angle of attack of 0° with increased Reynolds number. A comparison of these results with those for the single-slotted flap configuration presented in figure 29(a) indicates that the TE wedge produced a progressively smaller improvement in the maximum lift coefficient obtained with an increase in the number of flap elements. This lack of improvement may partially be due to the fact that part of the upper surface of the aft-flap element of the double-slotted flap system is normally separated at the maximum lift condition; therefore, the increased camber produced by the lower surface TE wedge only tends to increase the amount of separation, thus reducing the stall angle and maximum lift.

Small-Vane Configuration With Slat and Double-Slotted Flap

The effect of Reynolds number on the lift performance of the small-vane, high-lift configuration equipped with the baseline slat and the double-slotted flap is presented in figure 37. The trends observed in these data are different from those for the similarly equipped large-vane configuration shown in figure 34(b), which showed a gradual increase in maximum lift coefficient between Reynolds numbers of 3 and 8×10^6 and only a small change in the lift coefficient at an angle of attack of 0°. However, the data for the small-vane configuration presented in figure 37(b) show only a slight increase in maximum lift coefficient with increased Reynolds number and an unexpected gradual decrease in the lift coefficient at an angle of attack of 0° between Reynolds numbers of 6 and 12×10^6. As shown in figure 37(a), the slope of the lift coefficient versus angle-of-attack curve has a noticeable decrease at an angle of attack of 8° for the lower Reynolds number of 2.8×10^6.

The pitching-moment-coefficient data presented in figure 38 provide some insight into what occurred on the airfoil at the upper and lower bounds of the Reynolds number range. At angles of attack below 12° and at the highest Reynolds number of 20.9×10^6, the pitching-moment coefficient is less negative, a result indicating that slat loading increased <u>without</u> a corresponding increase in the vane/flap loading. This trend is similar to that which occurred for the large-vane configuration shown in figure 36 with the slat deflected -30°. At angles of attack above 12°, the pitching-moment coefficient shown in figure 38 is more negative and the slope of the lift coefficient versus angle-of-attack curve (lift-curve) remains linear, an effect indicating the reversed trend of an increase in slat loading <u>with</u> a corresponding increase in vane/flap loading.

It is expected that the lift performance trends observed during these two-dimensional tests would carry over into tests of a three-dimensional configuration with the same flap system. Therefore, determining the wing area based on low Reynolds number test results would predict that the full-scale aircraft could obtain the desired stall speed, which is based primarily on maximum lift. On the other hand, the test results at high Reynolds number indicate that it would require a noticeable increase in angle of attack to obtain the desired approach speed, which is based on a percentage of the maximum lift.

The effects of Reynolds number on the position optimization of the baseline slat are presented in figures 39 and 40. As shown in figure 39, the maximum lift coefficient decreased with increased slat deflection at the lower Reynolds number of 2.8×10^6, but at a Reynolds number of 12×10^6 the highest maximum lift coefficient occurred at a slat deflection of -24°. The results presented in figure 40 show that an increase in Reynolds number resulted in very little change in the optimum overlap position, but that the optimum gap setting increased from 2- to 3-percent chord with a corresponding increase of 0.08 in the maximum lift coefficient obtained. In general, it is expected that small, not larger, gap settings would be required at the higher Reynolds numbers to maintain the same mass-flow rates through the slots between elements because the slot boundary layers are thinner at the higher Reynolds numbers and, therefore, the effective gap is larger. These data again demonstrate the importance of conducting wind-tunnel tests of high-lift airfoils as close as possible to full-scale flight conditions.

The effect of Mach number on the maximum lift performance of the small-vane configuration with the baseline slat and double-slotted flap is presented in figure 41 for several different Reynolds numbers and gap settings. These data show a decrease

in maximum lift coefficient with increased Mach number for all conditions tested except for a Reynolds number of 12×10^6 and a gap of 3-percent chord, which shows a puzzling slight increase in maximum lift coefficient. As previously discussed for the large-vane cruise configuration, the compressibility effects associated with increased Mach number cause the laminar boundary layer on the leading-edge slat to detach at lower angles of attack and the corresponding lift to decrease. This effect explains the data trend except for the aforementioned gap of 3-percent chord and Reynolds number of 12×10^6; no explanation is offered for this unusual behavior. In the data presented in figure 41, also note the very rapid decrease in maximum lift coefficient with increased Mach number at a gap setting of 2.5-percent chord and a Reynolds number of 12×10^6 compared with the increase in maximum lift coefficient at a gap setting of 3-percent chord.

The effects of Reynolds number on the lift performance of the small-vane, high-lift configuration equipped with the large-chord slat and the double-slotted flap are presented in figure 42. The results of the slat deflection and gap position optimizations are presented in figure 43 and show that the optimum gap was 2-percent chord and the optimum slat deflection was -26° at both Reynolds numbers tested, which is different from the trend observed for the same configuration with the baseline slat shown in figures 39 and 40. The trend in lift performance data presented in figure 42 is similar to that for the baseline slat data presented in figure 37 with the exception of the behavior of the lift-curve slope at the low Reynolds number. A comparison of the lift performance data presented in figures 37(a) and 42(a) shows that the lift-curve slope breaks at a slightly lower angle of attack of 6° and that the rate of change in the lift-curve slope is less for the large-chord slat than for the baseline slat. Although the chord of the large-chord slat is 50 percent greater than that of the baseline slat, the maximum lift coefficient increased only by approximately 0.1, which represents an improvement of less than 3 percent.

The effects of Reynolds number on the lift performance of the small-vane, high-lift configuration equipped with the large-radius slat and the double-slotted flap are presented in figure 44. The results of the slat deflection and gap position optimization are presented in figure 45 and show results similar to those obtained for the baseline slat presented in figures 39 and 40. As shown in figure 45, the optimum slat deflection and gap setting increased with increased Reynolds number, a trend similar to that observed for the baseline slat. The effect of increased vane/flap deflection at Reynolds numbers of 2.8 and 12×10^6 is also presented in figure 45. These data show that the maximum lift coefficient increased by approximately 0.2 with the increase in Reynolds number. The trend in the lift performance data presented in figure 44 is similar to that observed for the large-chord slat presented in figure 42 and for the baseline slat presented in figure 37 with the exception of the behavior of the lift-curve slope at the low Reynolds number. The angle of attack corresponding to the break in the lift-curve slope for the large-radius slat is the same as that for the large-chord slat, and the rate of change of the lift-curve slope following the break is similar to that for the baseline slat. The maximum lift coefficient values obtained were almost identical for the large-chord and large-radius slat configurations.

The effects of placing a transition strip on the upper surface of the baseline slat of the small-vane, high-lift configuration are presented in figure 46 for Reynolds numbers of 2.8 and 12×10^6. The strip consisted of No. 120 grit and was located at about 5 percent of the slat chord. The data presented in figure 46 show the expected result of a decrease in maximum lift coefficient with the strip on. The decrease in maximum lift coefficient, which is slightly greater at the higher

Reynolds number, is probably due to the loss of laminar flow on the slat; this loss further thickens the turbulent boundary layer on the downstream main and flap elements inducing an earlier separation on the flap. The transition strip has no effect on the lift performance characteristics below the stall angle of attack.

Many wind-tunnel tests of high-lift airfoils and wings are conducted in atmospheric facilities that can obtain higher Reynolds number only by increasing the free-stream Mach number. To illustrate the error of testing in this manner to determine the effects of Reynolds number on lift performance, the small-vane, high-lift flap configuration with the baseline slat and double-slotted flap was tested by varying the tunnel total pressure and Mach number to maintain a constant Reynolds number of 4.9×10^6. These test results, presented in figure 47, show a decrease in the lift coefficient of approximately 0.25 at the lower angles of attack, a reduction in the stall angle of approximately 8°, and a corresponding reduction in the maximum lift coefficient of 0.5. Many wind-tunnel facilities also do not have sidewall BLC capability for use during high-lift airfoil testing, a deficiency which may cause an even greater loss in maximum obtainable lift coefficient.

Small-Vane Cruise Configuration With Simulated Frost and Glaze Ice

The effects of Reynolds number on the maximum lift performance of the small-vane cruise configuration with simulated frost and glaze ice on the leading edge are presented in figure 48. These data show that the part-frost configuration produced approximately 23 percent less maximum lift coefficient than the clean leading-edge configuration and that the full-frost configuration produced approximately 27 percent less maximum lift coefficient. The frost, which is simulated by a very coarse No. 70 grit, prevents the development of a laminar boundary layer on the leading edge even though a favorable pressure gradient exists. However, the turbulent boundary layer that does exist is very thick and unable to remain fully attached to the trailing edge at very high angles of attack. The simulated glaze ice configuration produced about 40 percent less maximum lift coefficient than the clean leading-edge configuration. The glaze ice shape not only ensured fully turbulent flow on both surfaces but also further reduced the maximum lift by decreasing the effective leading-edge camber. An increase in Reynolds number had only minor effects on the variation of maximum lift coefficient for either the simulated frost or glaze ice configurations, a result which is not surprising in view of the fact that all surface boundary layers are fully turbulent.

CONCLUDING REMARKS

The experimental test results for the large- and small-vane, cruise and high-lift airfoil configurations have demonstrated the tremendous effects that Reynolds number and Mach number have on the lift performance. The performance of the high-lift airfoil configurations was very strongly influenced by the positioning of the leading-edge slat which protects the leading edge of the main element by lowering its leading-edge suction peak and by injecting high-energy air through the slot between the elements to thin and delay the separation of the boundary layer on the downstream flap elements. Analysis of the test data has shown that trends observed with an increase in Reynolds number for the large-vane model were not identical to those observed for the small-vane model. One very interesting trend observed for the small-vane model was that the optimum gap setting for the leading-edge slat increased rather than decreased by approximately 50 percent with an increase in Reynolds number from 2.8 to 12×10^6.

The test results also indicated that some form of sidewall boundary-layer control is absolutely necessary to ensure spanwise uniformity of the flow near stall and maximum lift conditions. Analysis of the data showed that increasing the Mach number instead of increasing the tunnel total pressure to study the effects of increased Reynolds number can lead to completely erroneous and misleading results. The lift and pitching-moment coefficients determined by integration of the surface static pressure distributions compared very favorably with values measured by the force balance. Analysis of the drag data obtained with the downstream wake-rake traversing system demonstrated the detrimental effect of the slat and flap support brackets on spanwise uniformity of the multilayered wake for the high-lift airfoil.

NASA Langley Research Center
Hampton, VA 23665-5225
June 3, 1987

REFERENCES

1. McGhee, Robert J.; Beasley, William D.; and Foster, Jean M.: Recent Modifications and Calibration of the Langley Low-Turbulence Pressure Tunnel. NASA TP-2328, 1984.

2. Oliver, Wayne R.: Results of Design Studies and Wind Tunnel Tests of an Advanced High Lift System for an Energy-Efficient Transport. NASA CR-159389, 1980.

3. Omar, E.; Zierten, T.; Hahn, M.; Szpiro, E.; and Mahal, A.: Two-Dimensional Wind-Tunnel Tests of a NASA Supercritical Airfoil With Various High-Lift Systems. Volume II - Test Data. NASA CR-2215, 1977.

4. Bragg, M. B.; and Coirier, W. J.: Aerodynamic Measurements of an Airfoil With Simulated Glaze Ice. AIAA-86-0484, Jan. 1986.

5. Pope, Alan; and Harper, John J.: Low-Speed Wind Tunnel Testing. John Wiley & Sons, Inc., c.1966.

6. Pankhurst, R. C.; and Holder, D. W.: Wind-Tunnel Technique. Sir Isaac Pitman & Sons, Ltd. (London), 1965.

7. Crowder, J. P.; Hill, E. G.; and Pond, C. R.: Selected Wind Tunnel Testing Developments at the Boeing Aerodynamics Laboratory. A Collection of Technical Papers - AIAA 11th Aerodynamic Testing Conference, Mar. 1980, pp. 262-272. (Available as AIAA-80-0458.)

8. McGhee, Robert J.; and Beasley, William D.: Low-Speed Aerodynamic Characteristics of a 17-Percent-Thick Airfoil Section Designed for General Aviation Applications. NASA TN D-7428, 1973.

9. Beasley, William D.; and McGhee, Robert J.: Experimental and Theoretical Low-Speed Aerodynamic Characteristics of the NACA 65_1-213, a = 0.50, Airfoil. NASA TM X-3160, 1975.

10. Wootton, L. R.: The Effect of Compressibility on the Maximum Lift Coefficient of Airfoils at Subsonic Airspeeds. J. Royal Aeronaut. Soc., vol. 71, July 1967, pp. 476-486.
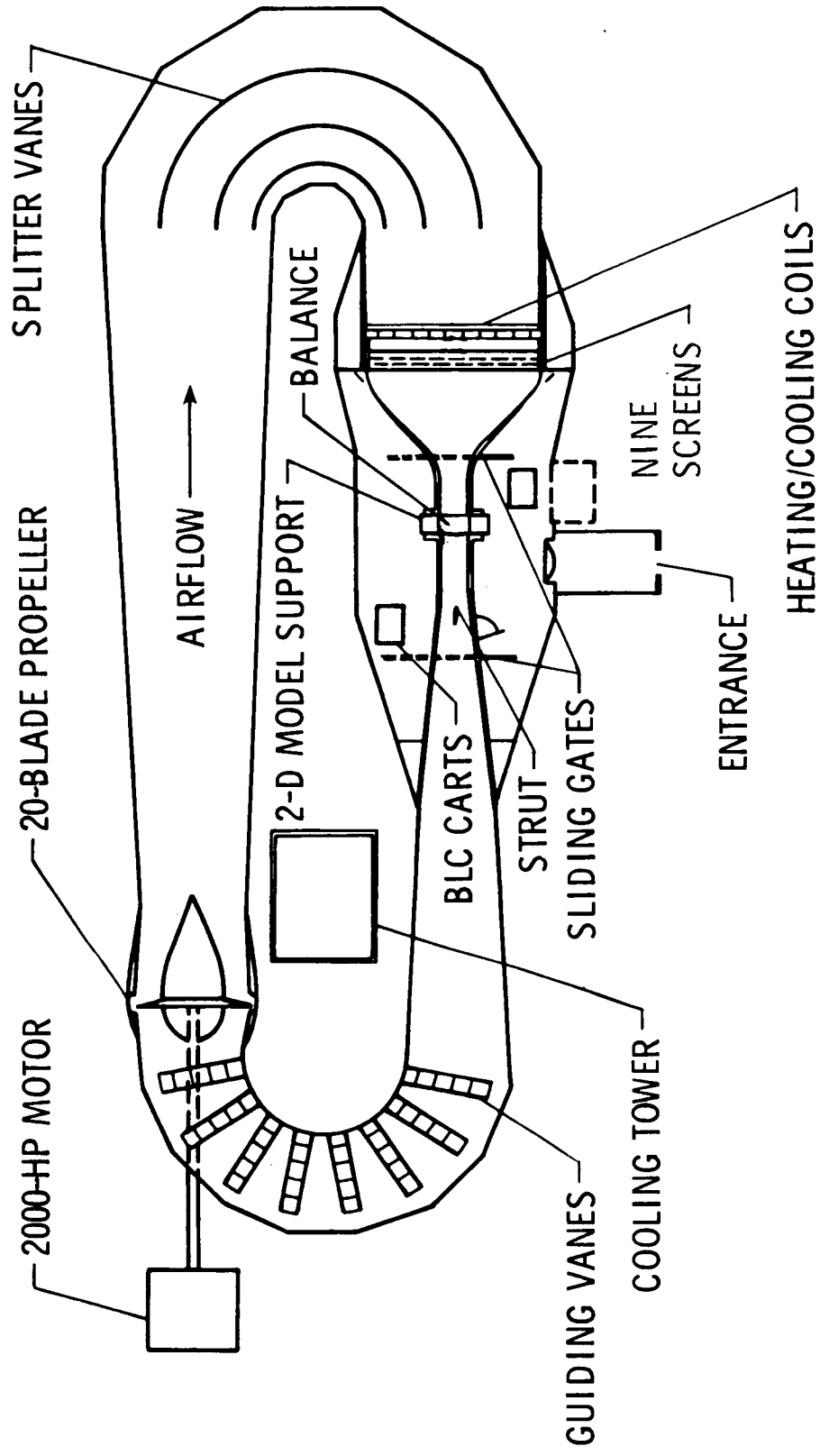
Figure 1.- Sketch of the Langley Low-Turbulence Pressure Tunnel (LTPT).

SPLITTER VANES

20-BLADE PROPELLER

AIRFLOW

2-D MODEL SUPPORT

BALANCE

BLC CARTS

STRUT

SLIDING GATES

ENTRANCE

NINE SCREENS

HEATING/COOLING COILS

2000-HP MOTOR

GUIDING VANES

COOLING TOWER
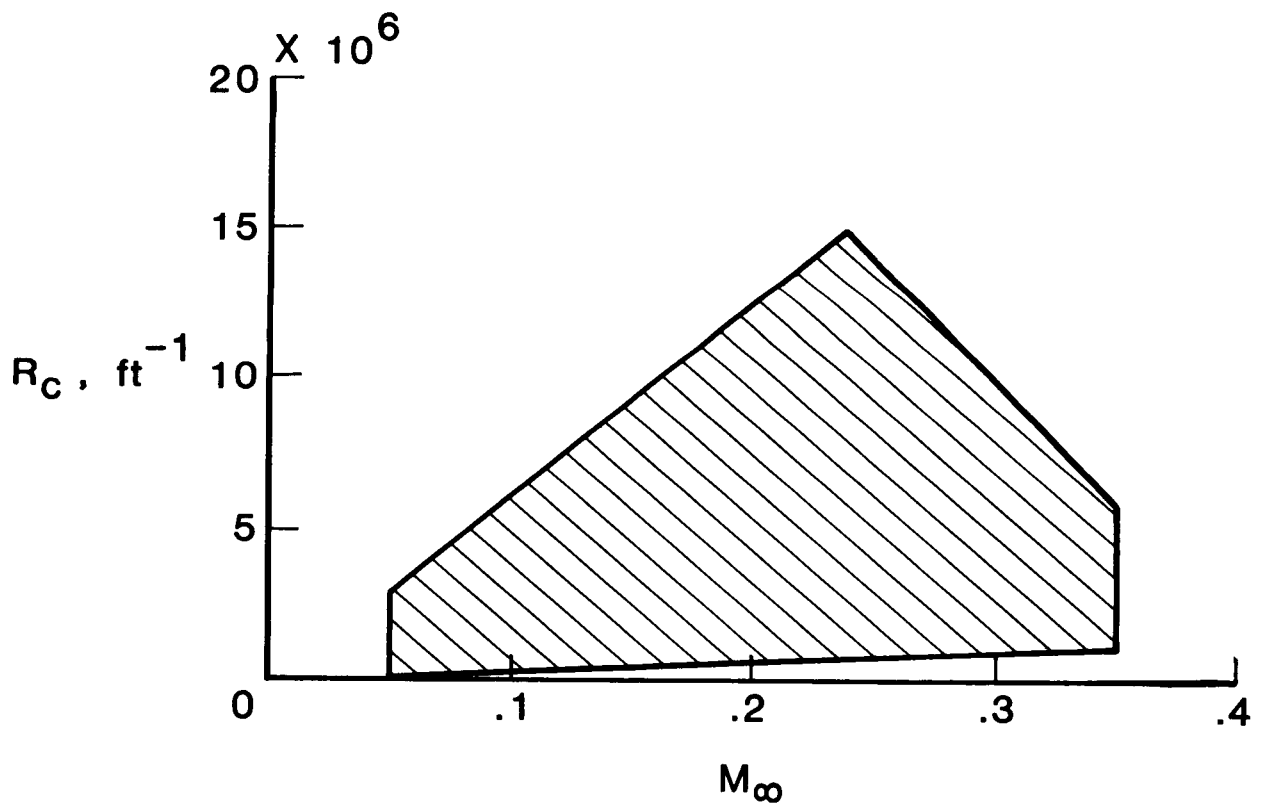
Figure 2.- Reynolds number capability of the LTPT.
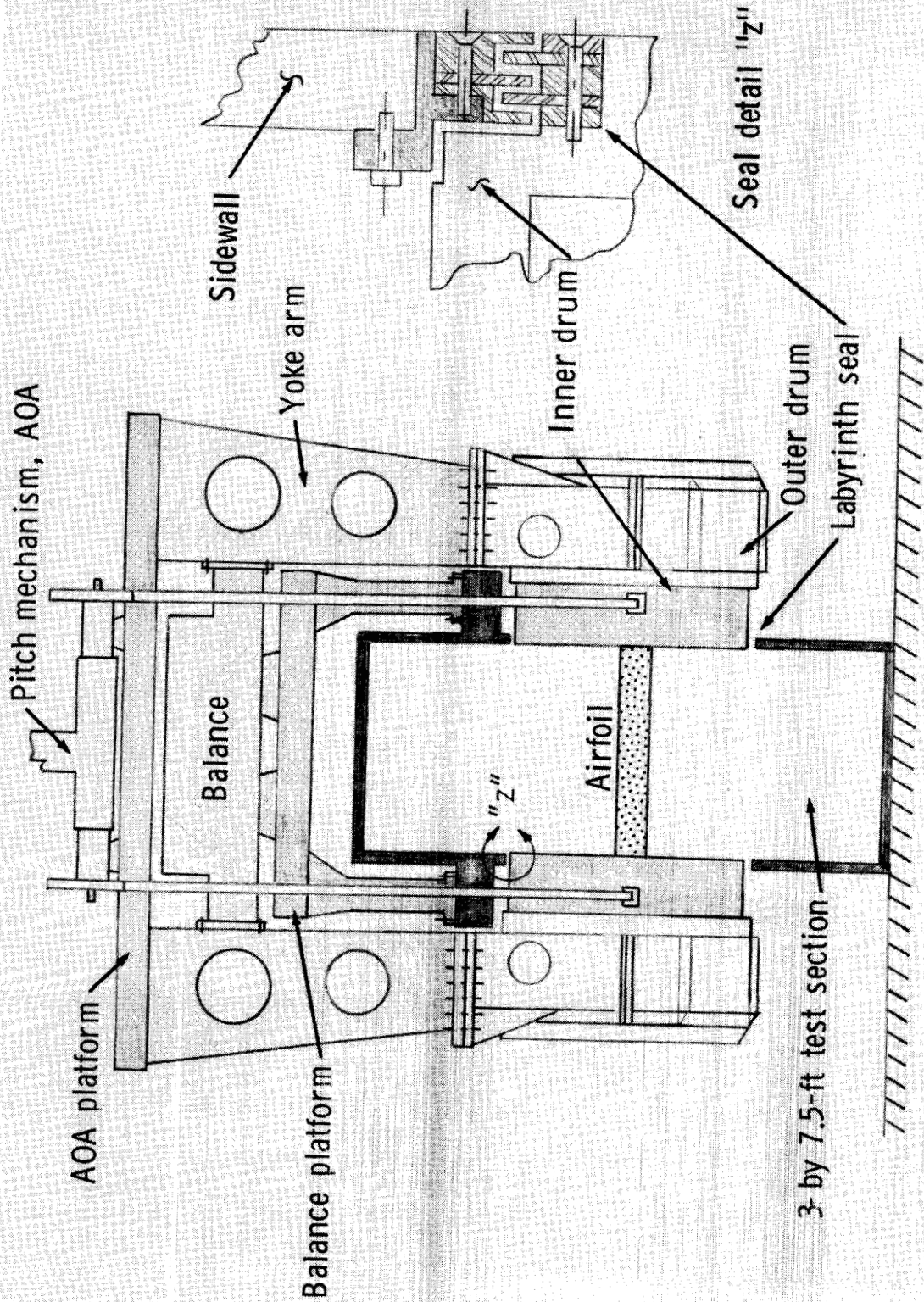
Figure 3.- Model-support and force-balance system for the Langley Low-Turbulence Pressure Tunnel. View looking upstream.
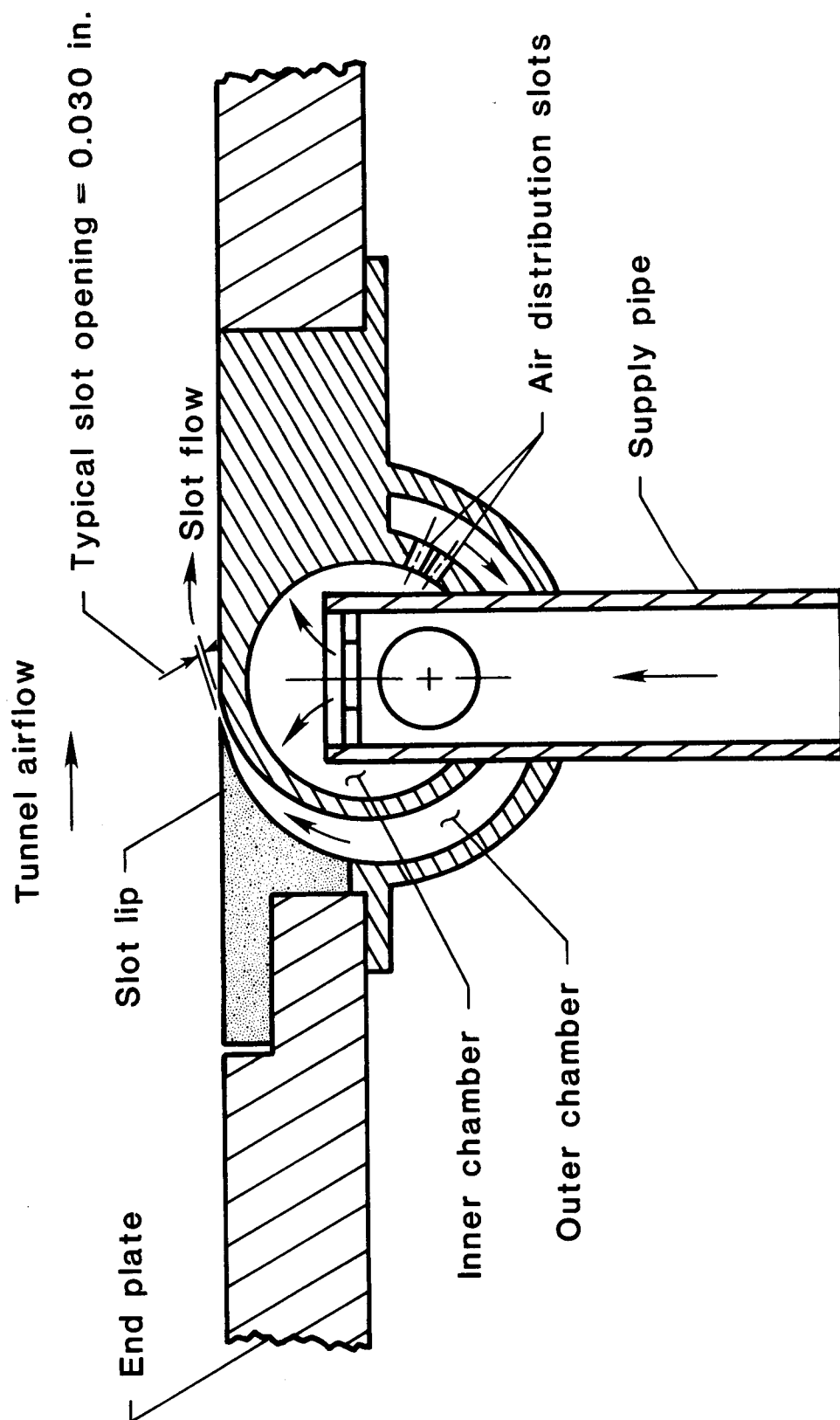
Figure 4.- Sketch of cross section of typical blowing box.
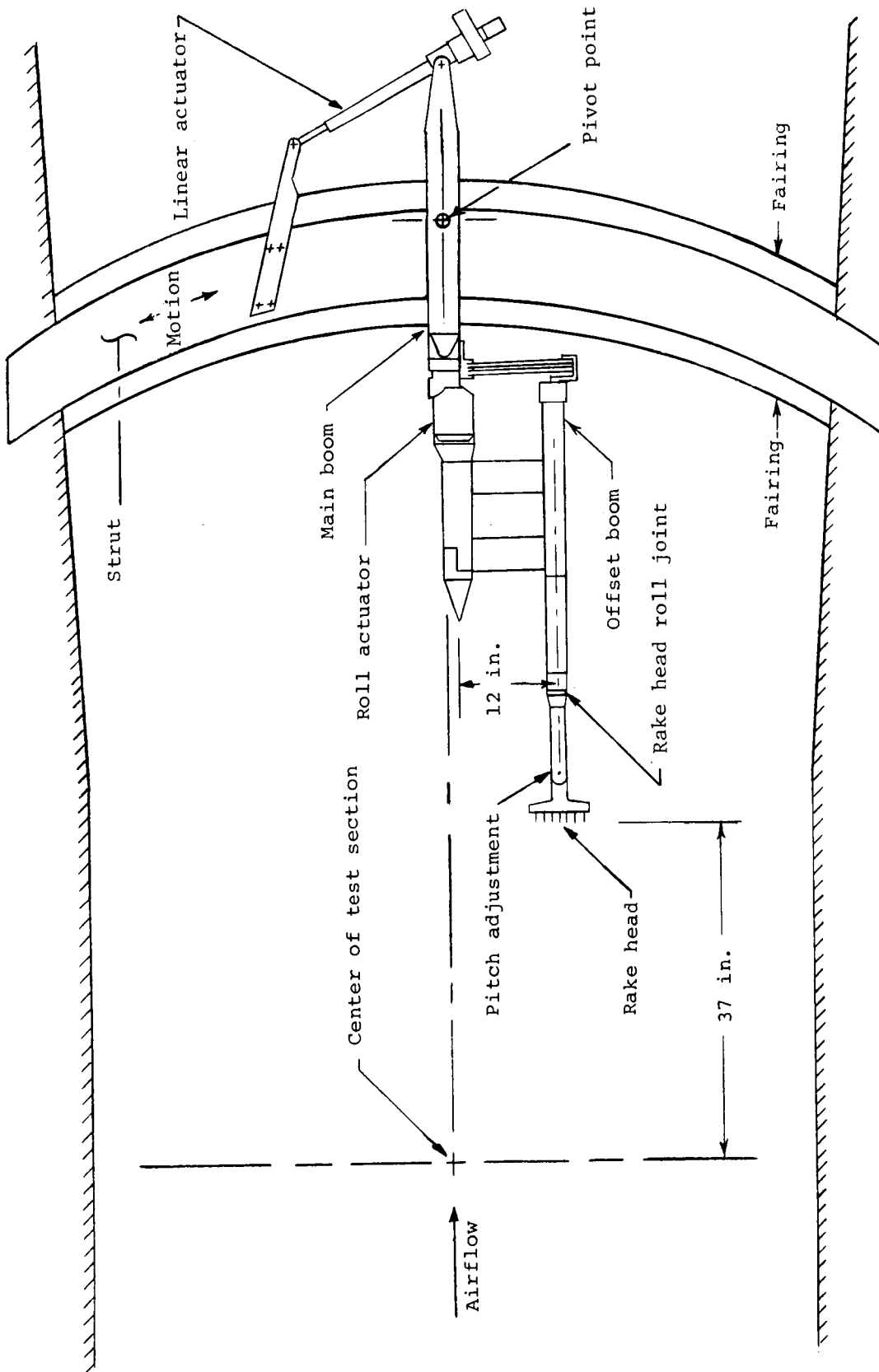
Figure 5.- Sketch of remote-controlled wake survey apparatus for the
Langley Low-Turbulence Pressure Tunnel.

23
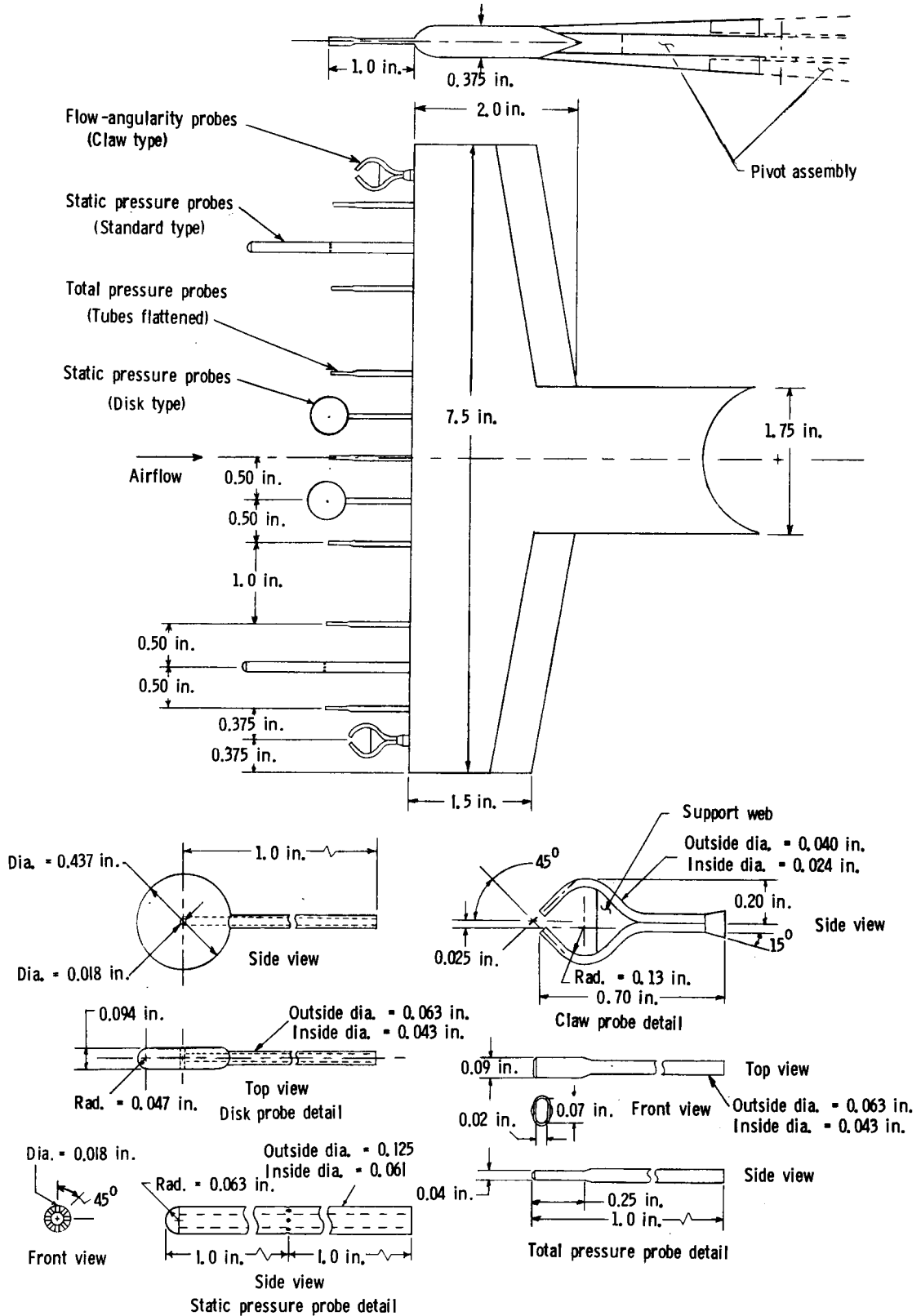
Figure 6.- Details of wake survey rake.
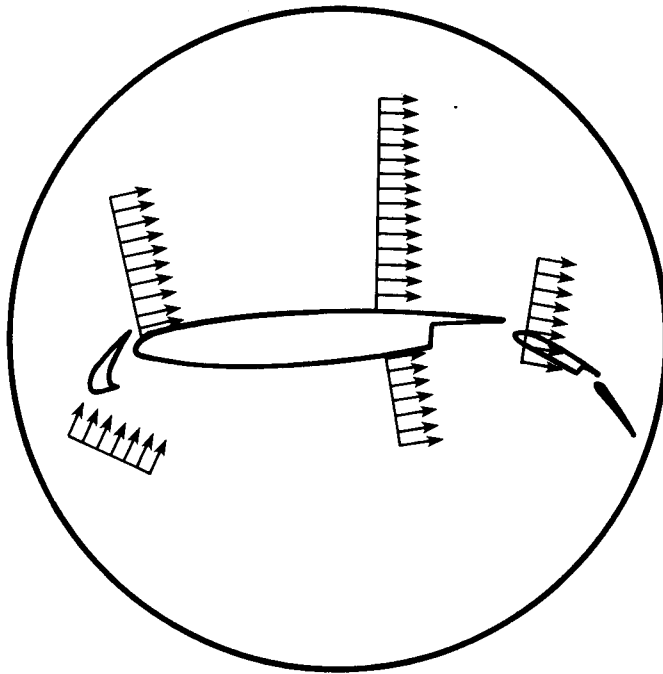
(a) Large-vane model.
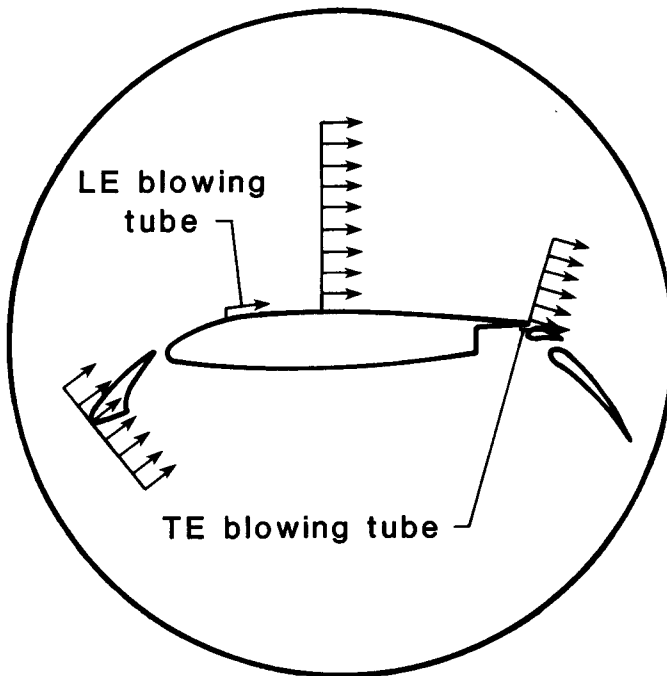
(b) Small-vane model.

Figure 7.- Geometry and blowing box locations for each model.
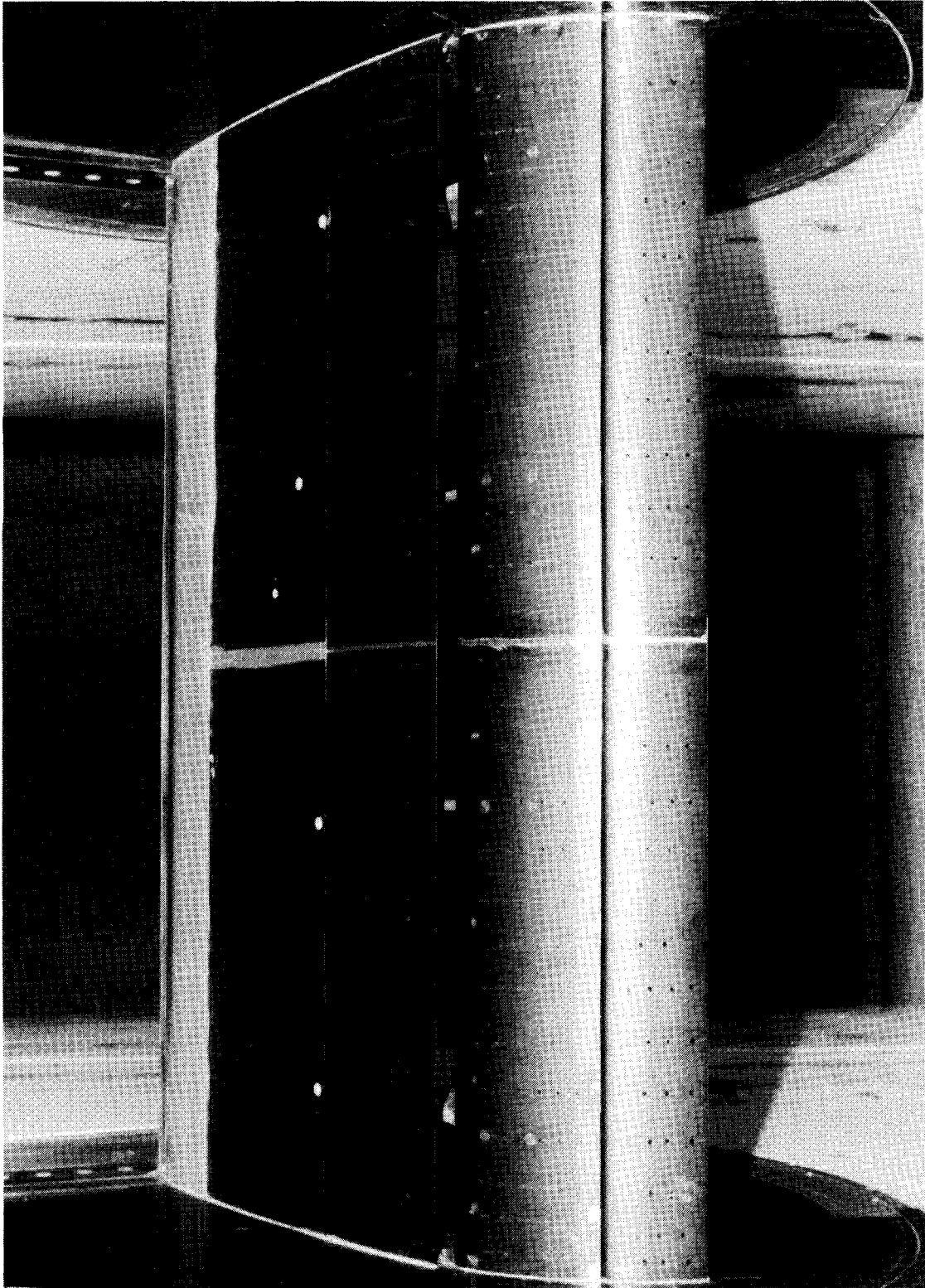
L-85-4424

(a) Full view.

Figure 8.- Photographs of upper surface of large-vane model in the LTPT. View looking upstream.
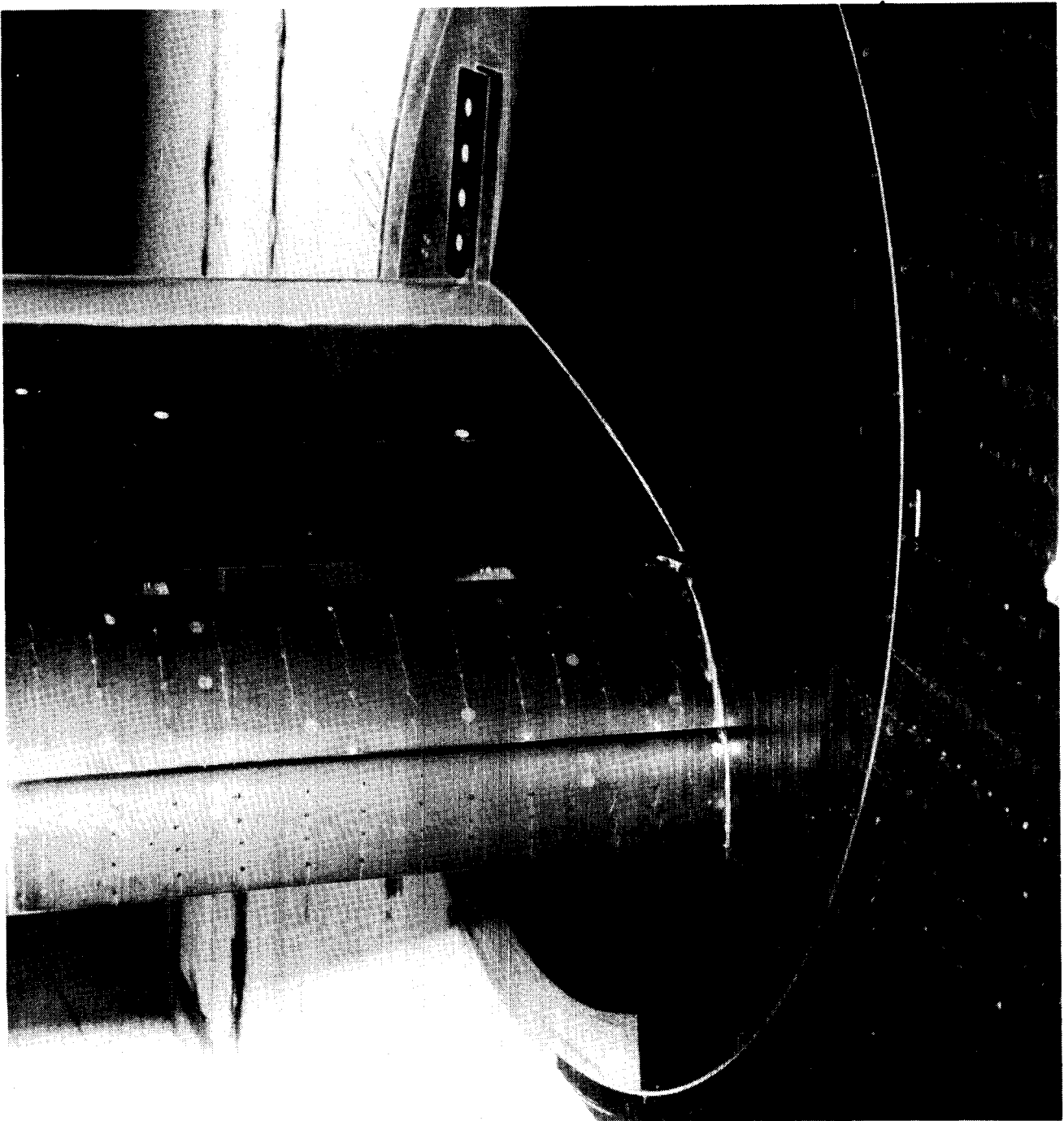
L-85-4423

(b) Juncture view.

Figure 8.- Concluded.
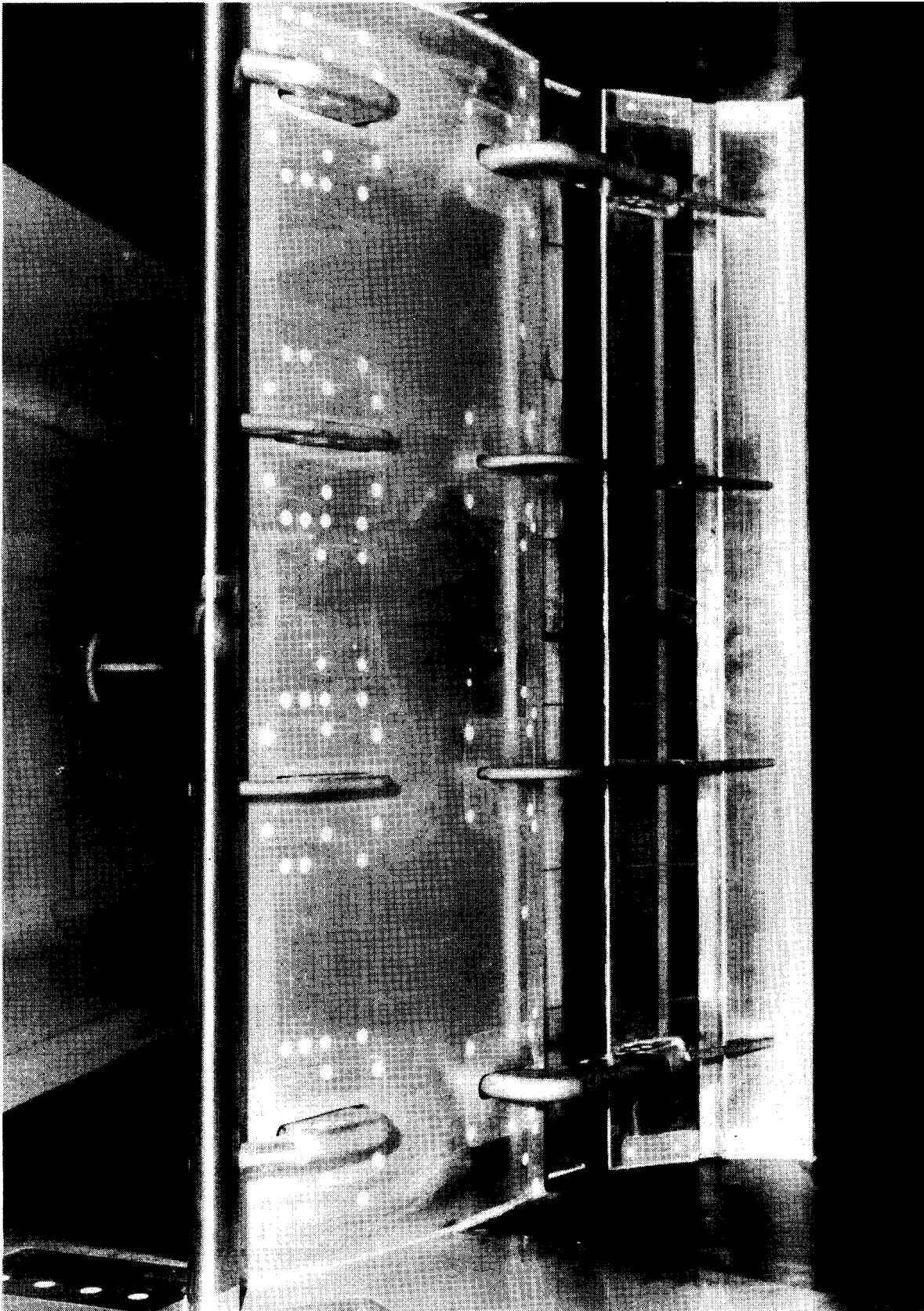
Figure 9.- Photograph of lower surface of large-vane model showing bracket arrangement. View looking downstream.

L-85-4425
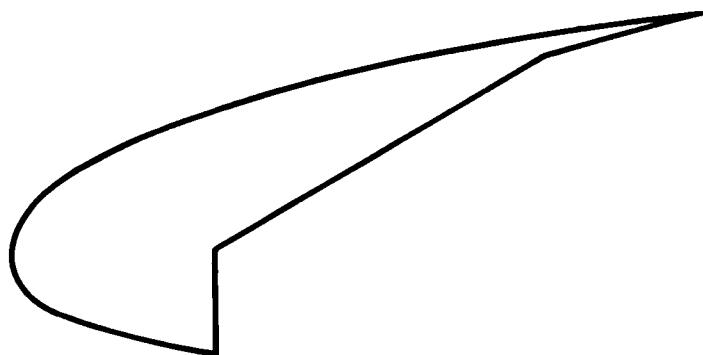
(a) Baseline slat with 13 percent chord.
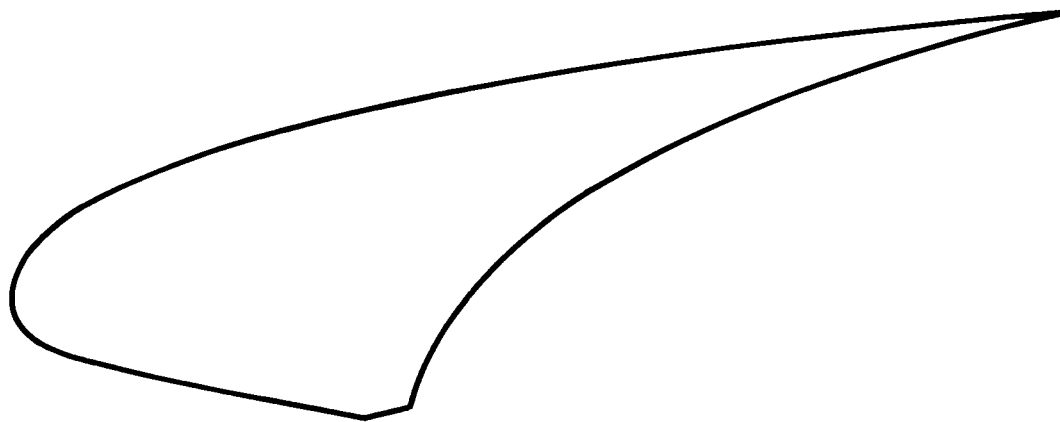
(b) Large-chord slat with 19.5 percent chord.
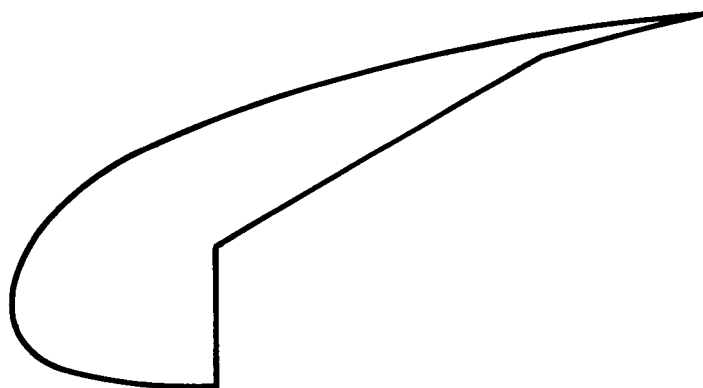
(c) Large-radius slat with 13 percent chord.

Figure 10.- Sketch of slat geometries for small-vane model.
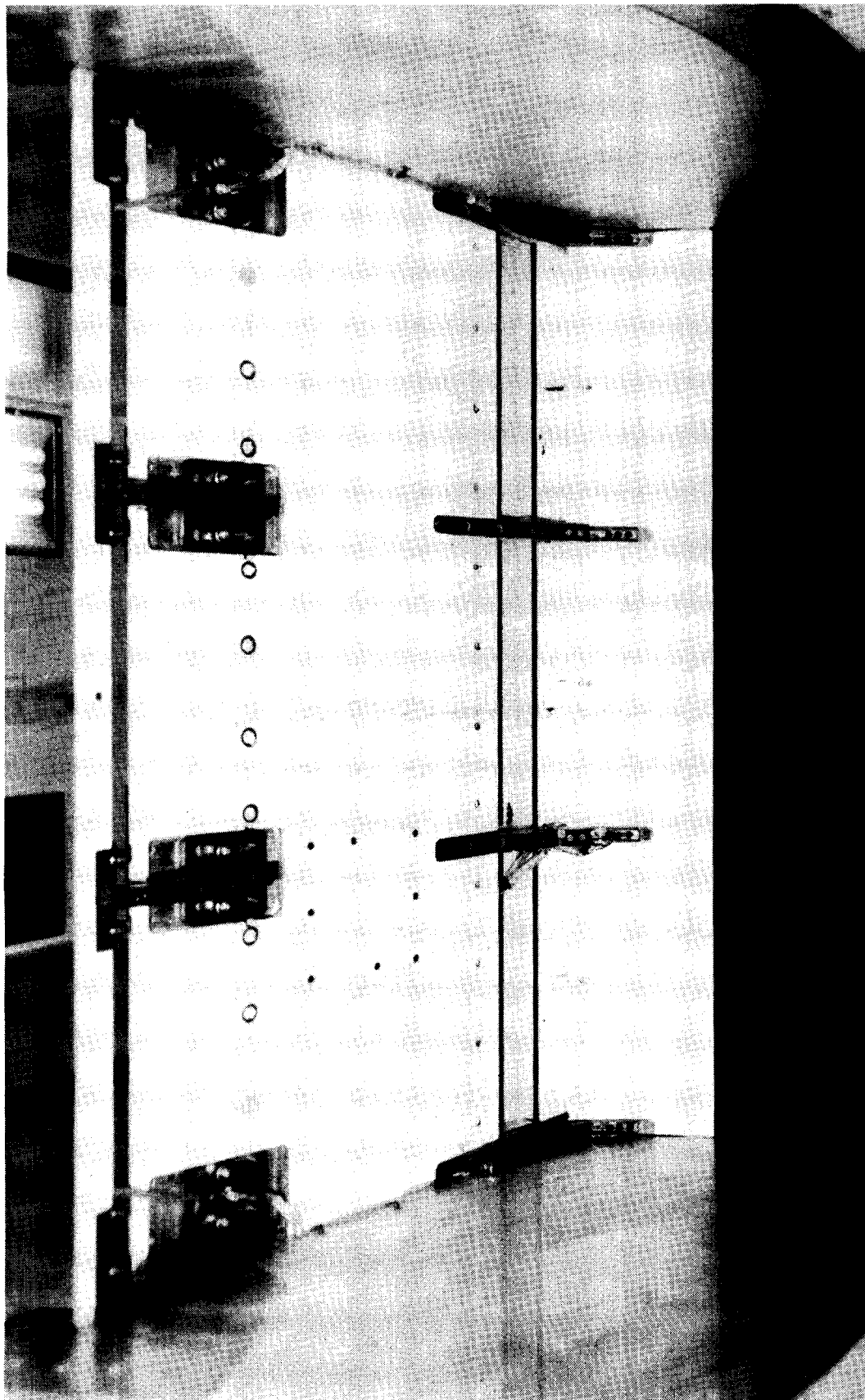
L-85-13,967

Figure 11.- Photograph of lower surface of small-vane model showing bracket arrangement. View looking downstream.
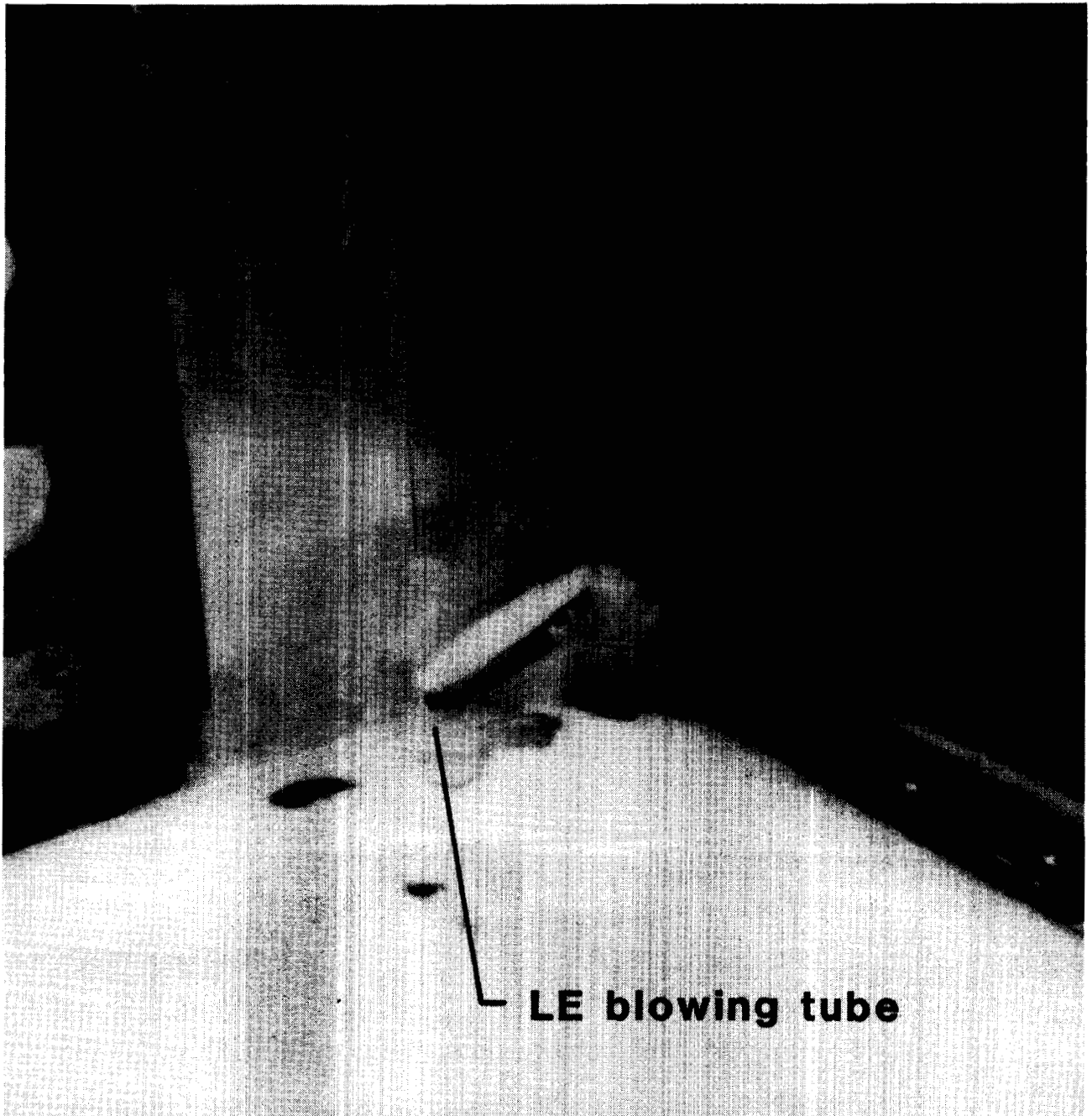
L-86-6312

Figure 12.- Photograph of leading-edge blowing tube on small-vane model.
View looking upstream.

31
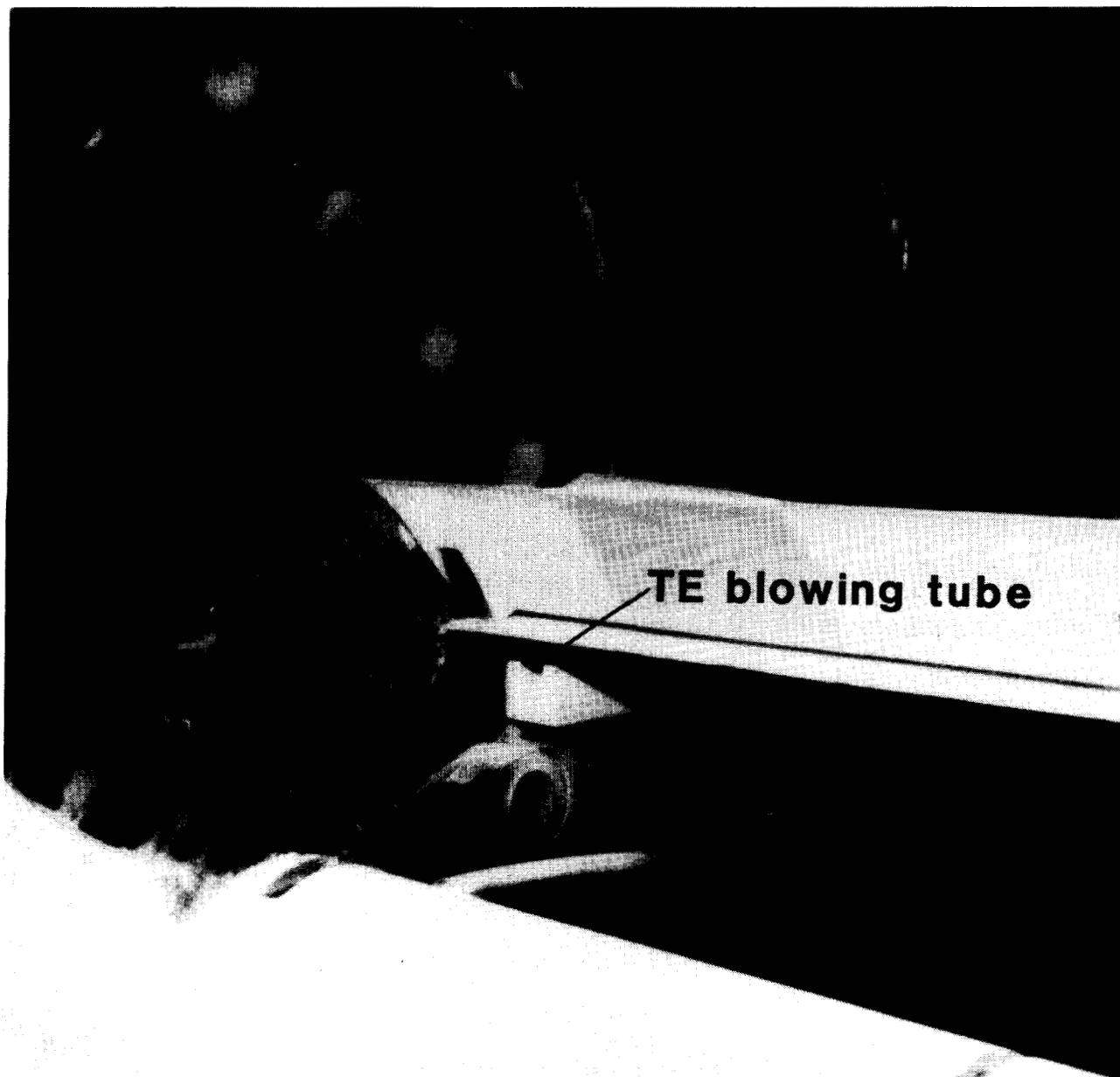
L-86-6313

Figure 13.- Photograph of trailing-edge blowing tube on small-vane model.
View looking upstream with vane removed to provide view of tube exit.

Simulated shape

Airfoil surface
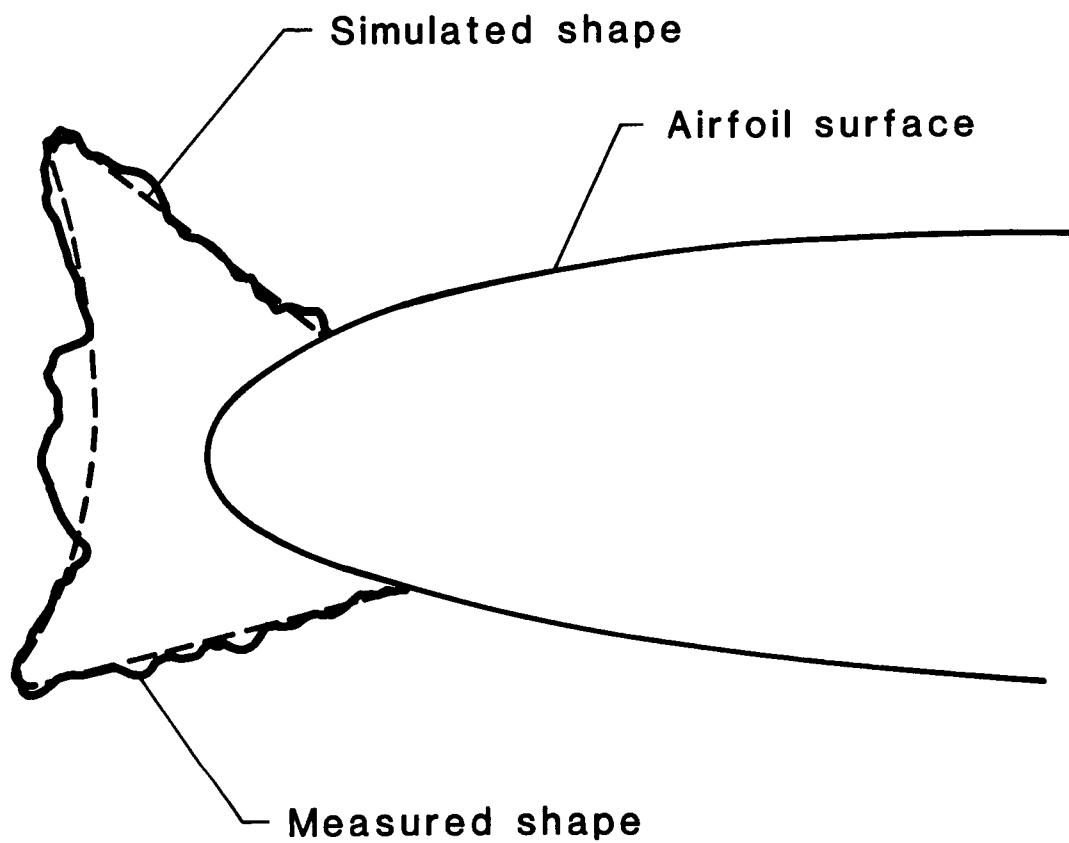
Measured shape

Figure 14.- Comparison between measured and simulated glaze
ice shapes for small-vane cruise airfoil.

L-86-6314

Figure 15.- Photograph of simulated glaze ice shape attached to leading edge of small-vane cruise airfoil. View looking downstream.
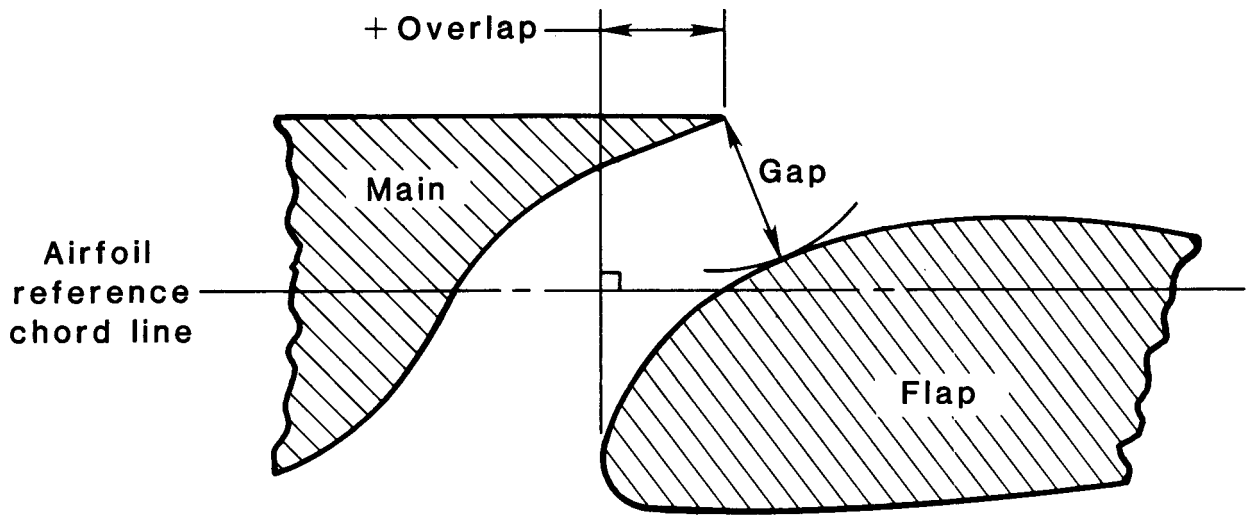
Figure 16.- Sketch illustrating definition of slat or flap overlap and gap.
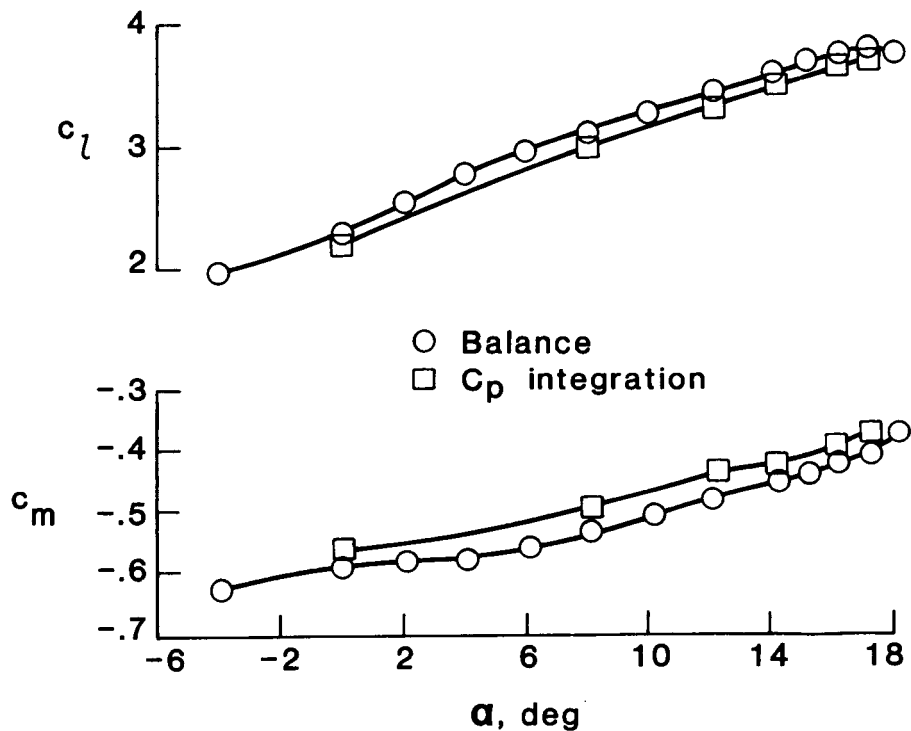
Figure 17.- Typical comparison between force balance and integrated surface pressure lift and pitching-moment coefficients for small-vane model with baseline slat and double-slotted flap deflected. $R_c = 12 \times 10^6$; $M_\infty = 0.2$; $\delta_s = -24°$; $\delta_{vf} = 45°$.
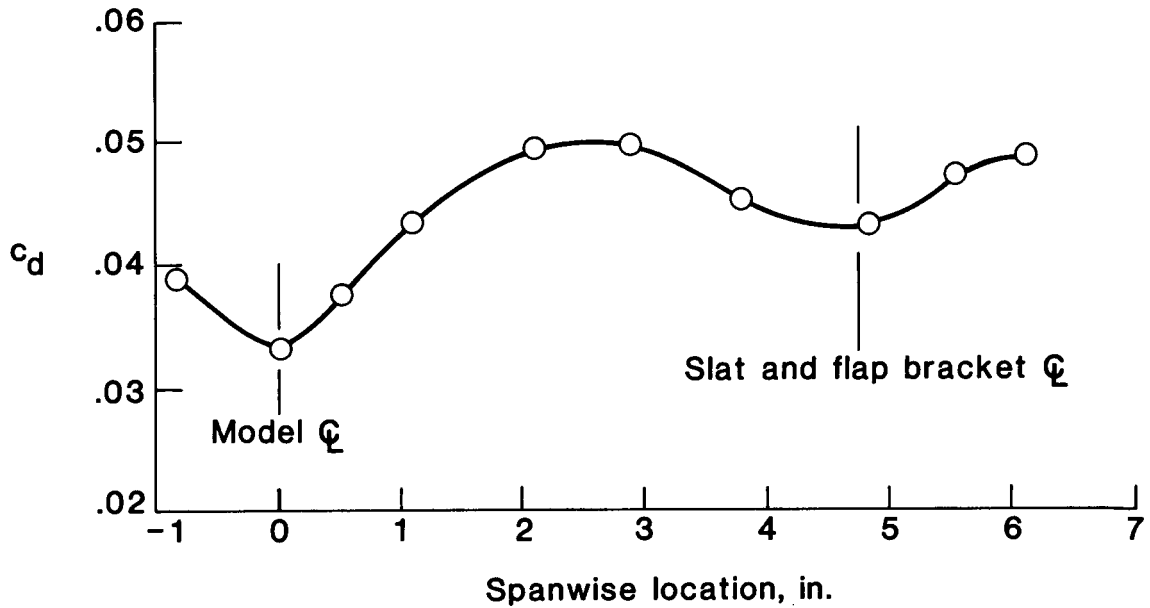
Figure 18.- Effect of slat and flap support brackets on spanwise variation of wake-measured drag for large-vane model with slat and double-slotted flap. $R_c = 3 \times 10^6$; $M_\infty = 0.2$; $\delta_s = -30°$; $\delta_v = 35°$; $\delta_f = 50°$.
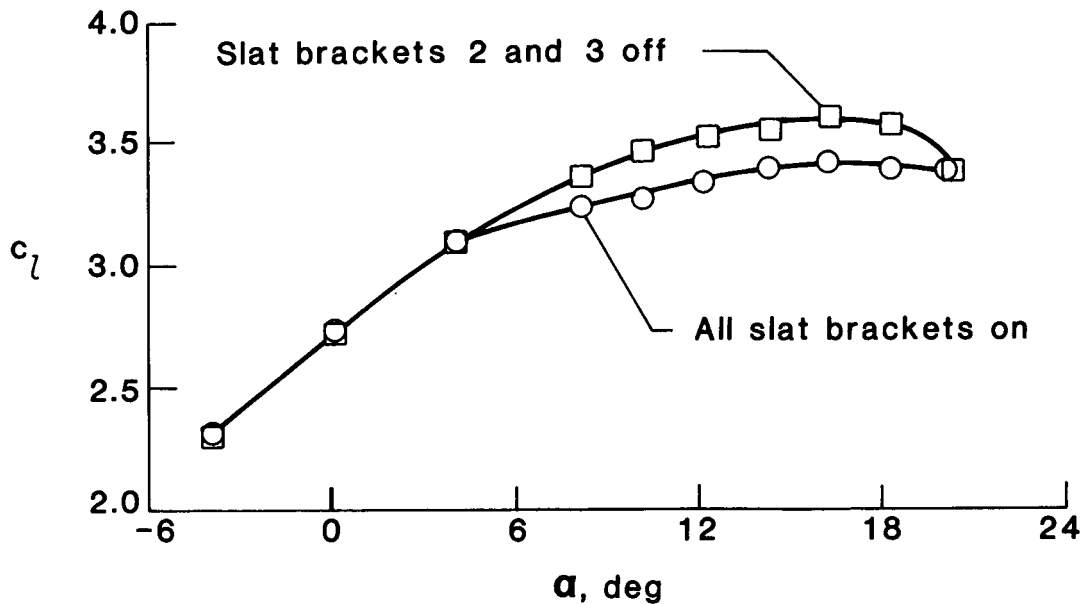
Figure 19.- Effect of slat support brackets on lift performance of small-vane model with baseline slat and double-slotted flap. $R_c = 2.8 \times 10^6$; $M_\infty = 0.2$; $\delta_s = -28°$; $\delta_{vf} = 45°$.
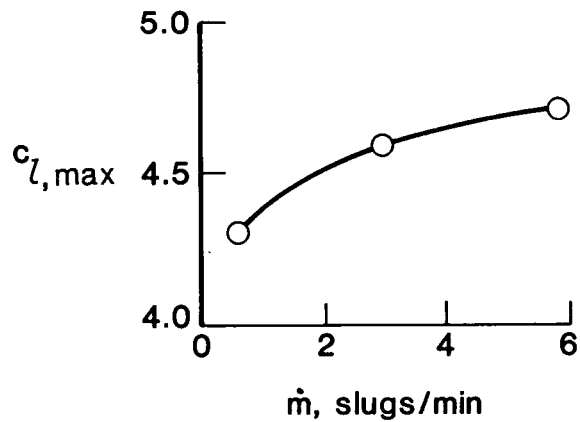
Figure 20.- Effect of total box mass-flow rate on maximum lift coefficient of large-vane model with slat and double-slotted flap. $R_c = 9 \times 10^6$; $M_\infty = 0.20$; $\delta_s = -30°$; $\delta_v = 35°$; $\delta_f = 50°$.
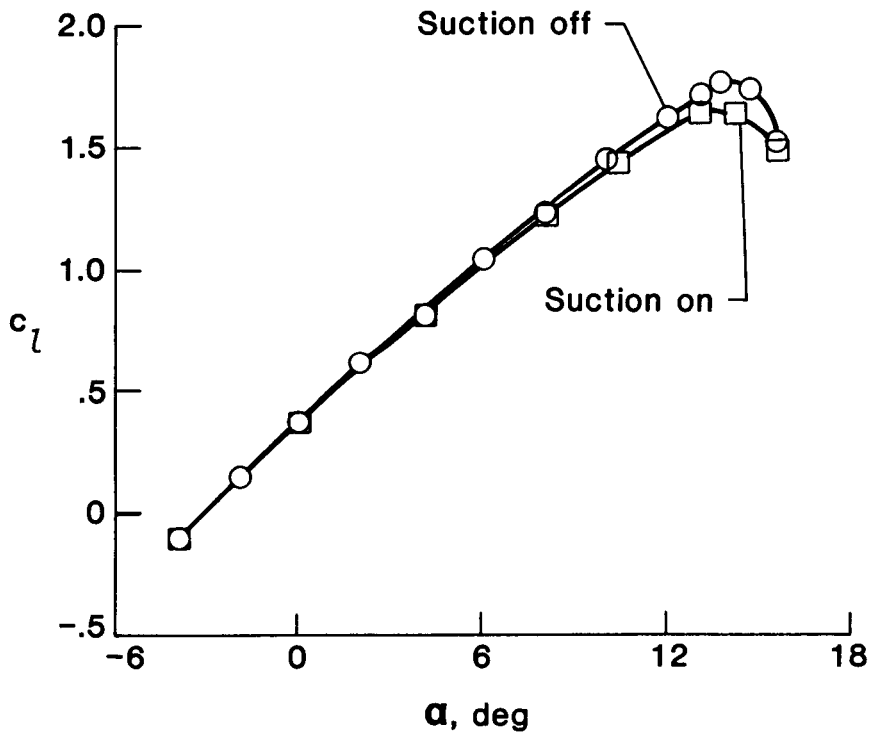
Figure 21.- Effect of upstream sidewall suction on lift performance of large-vane cruise configuration. All sidewall blowing boxes operated at maximum mass-flow rate. $R_c = 9 \times 10^6$; $M_\infty = 0.2$.
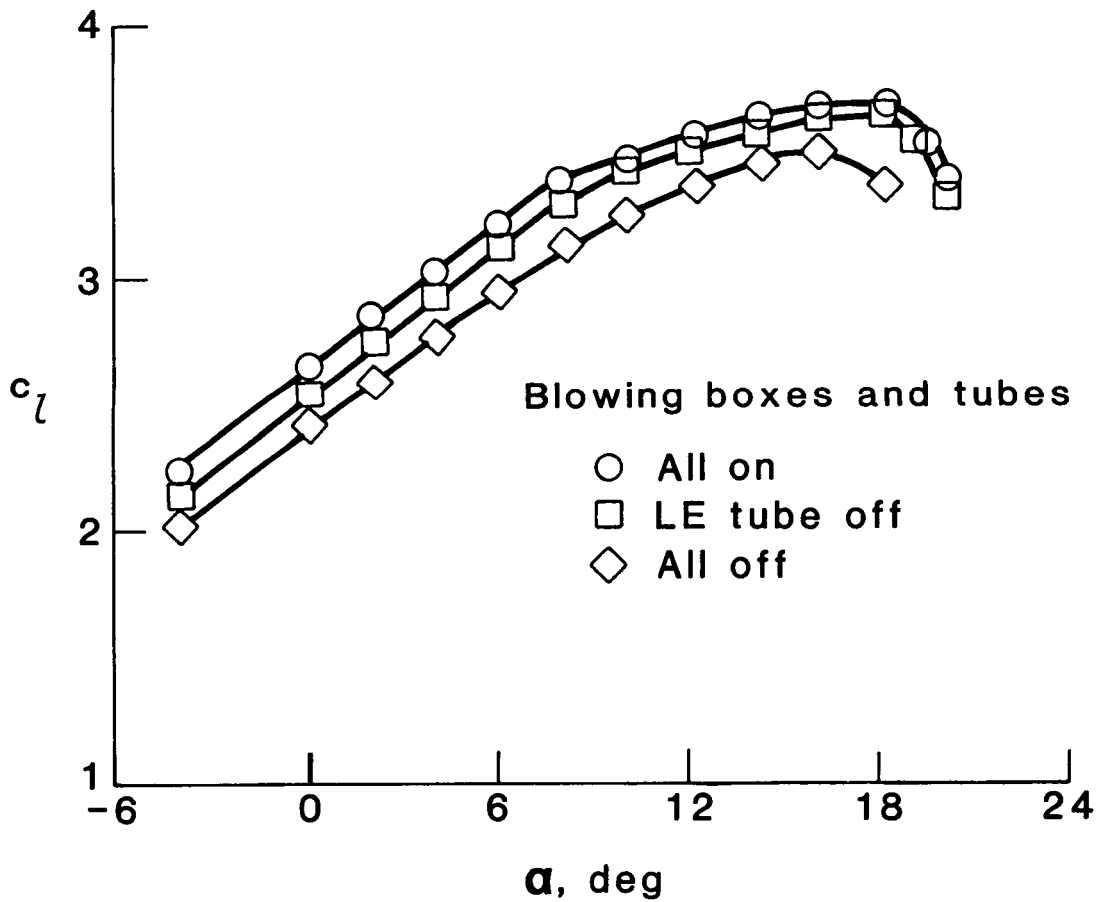
Figure 22.- Effect of sidewall blowing on lift performance
of small-vane model with baseline slat and double-
slotted flap. $R_c = 2.8 \times 10^6$; $M_\infty = 0.2$; $\delta_s = -24°$;
$\delta_{vf} = 45°$.
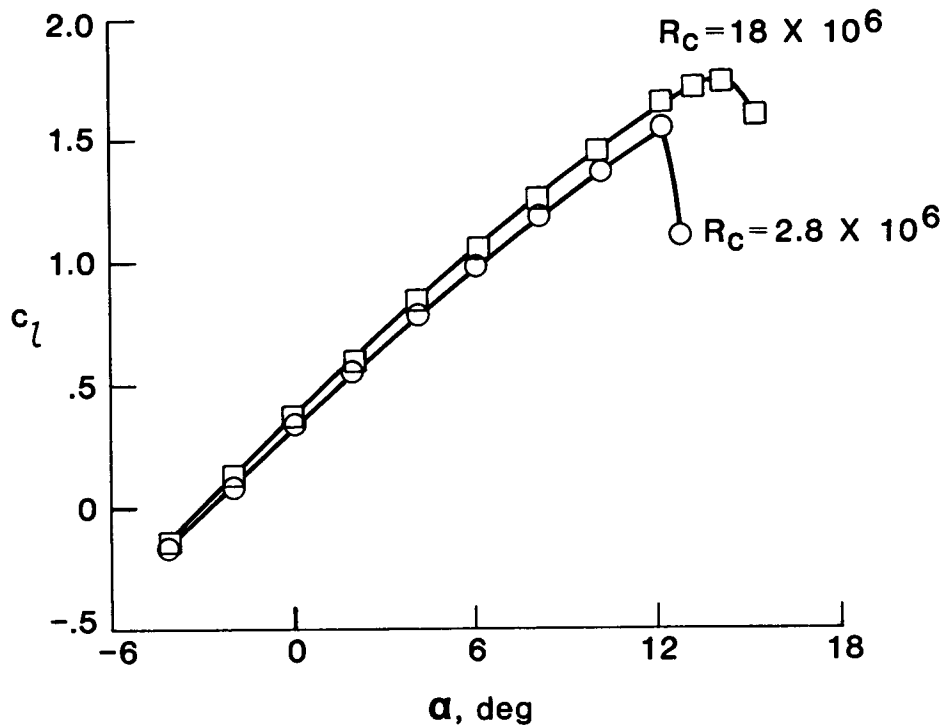
(a) Lift coefficient versus angle of attack.
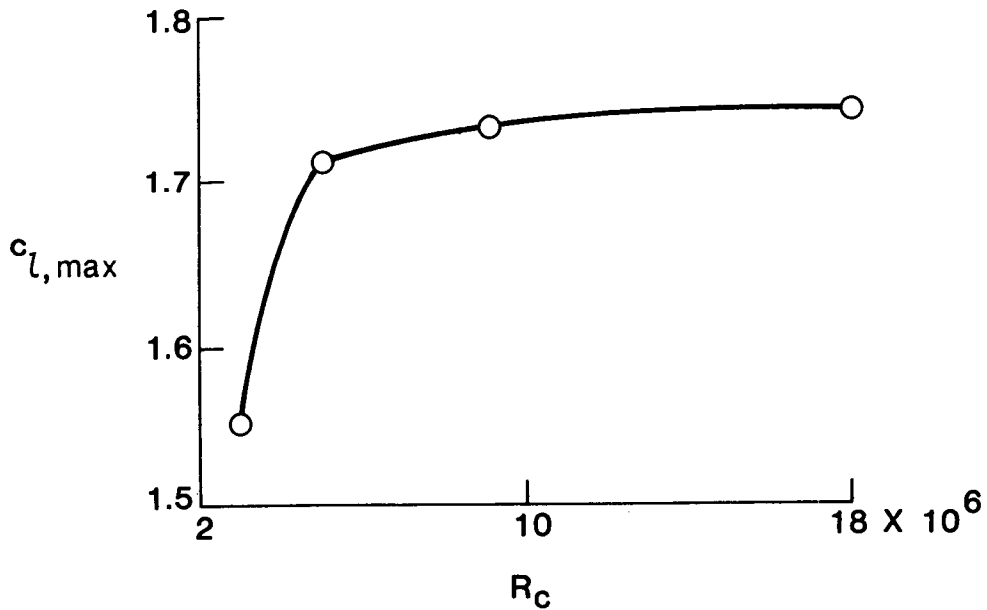
(b) Maximum lift coefficient versus Reynolds number.

Figure 23.- Effect of Reynolds number on lift performance of large-vane cruise airfoil. $M_\infty = 0.2$.
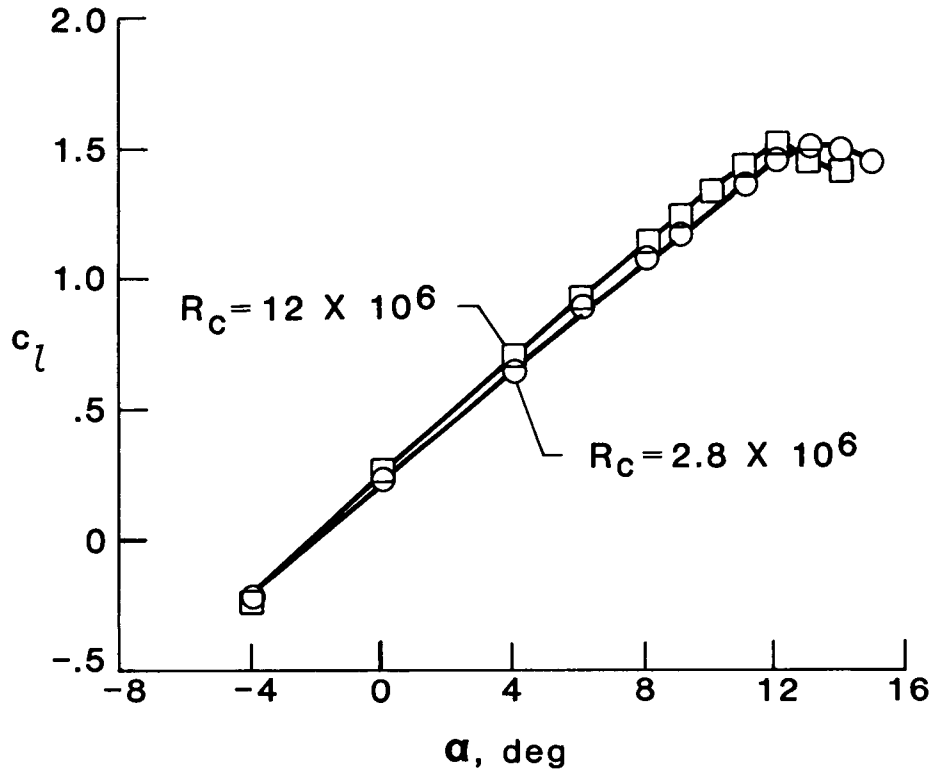
(a) Lift coefficient versus angle of attack.
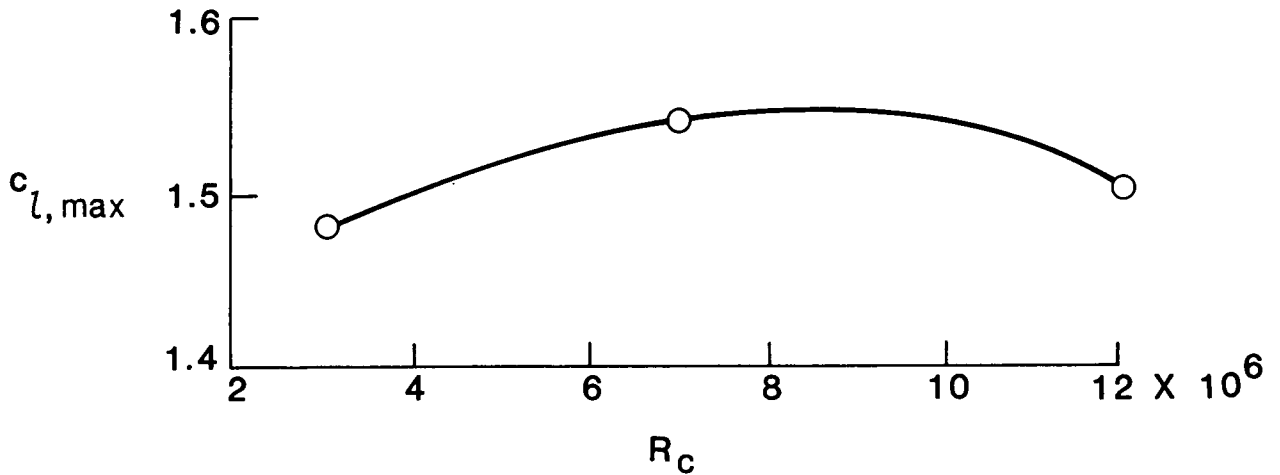
(b) Maximum lift coefficient versus Reynolds number.

Figure 24.- Effect of Reynolds number on lift performance of small-vane cruise airfoil. $M_\infty = 0.2$.
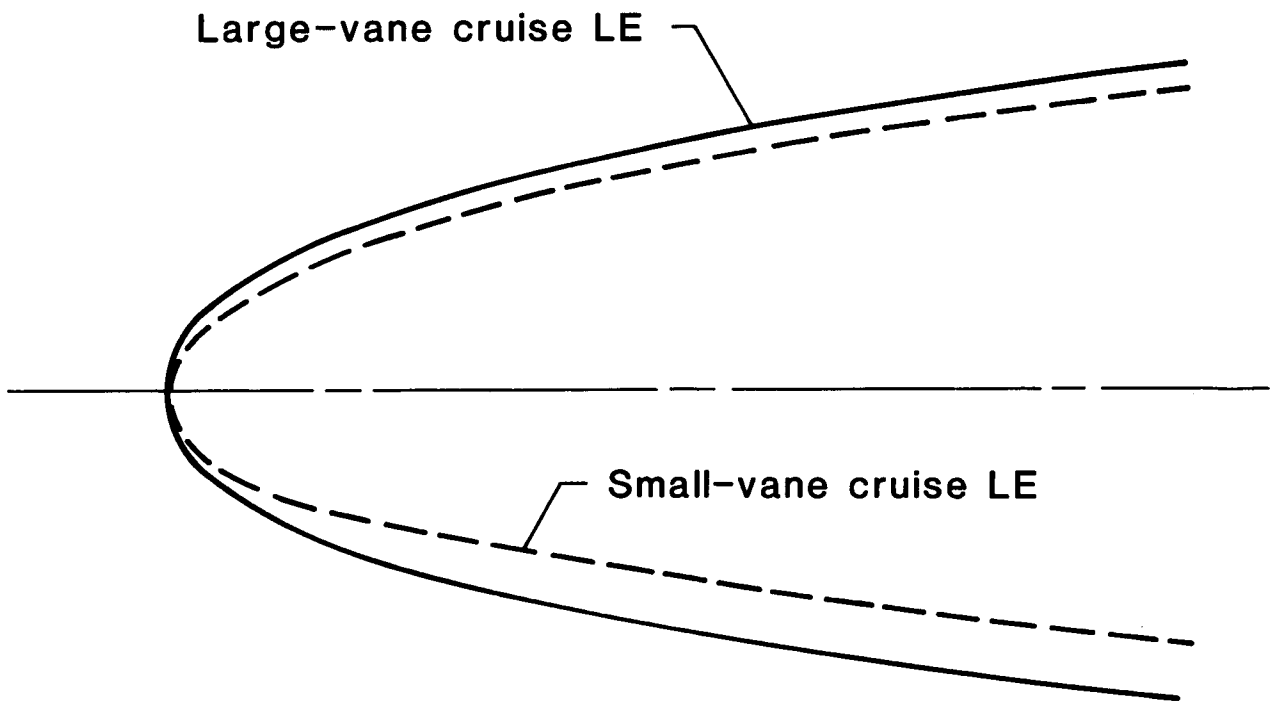
Figure 25.- Comparison of leading-edge geometries for small- and large-vane cruise airfoils.
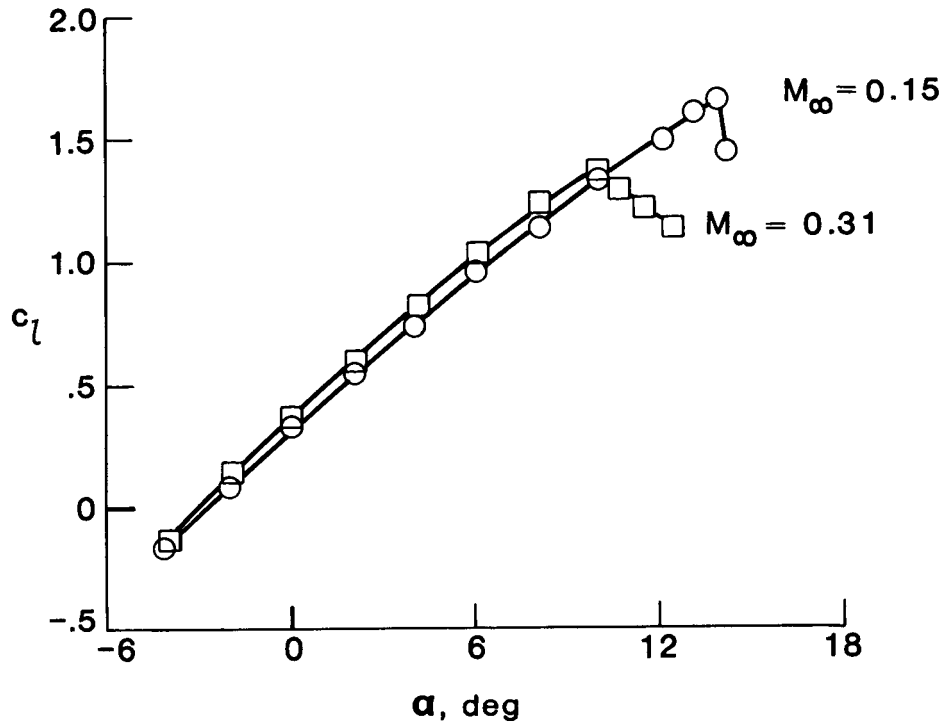
(a) Lift coefficient versus angle of attack. $R_c = 3 \times 10^6$.
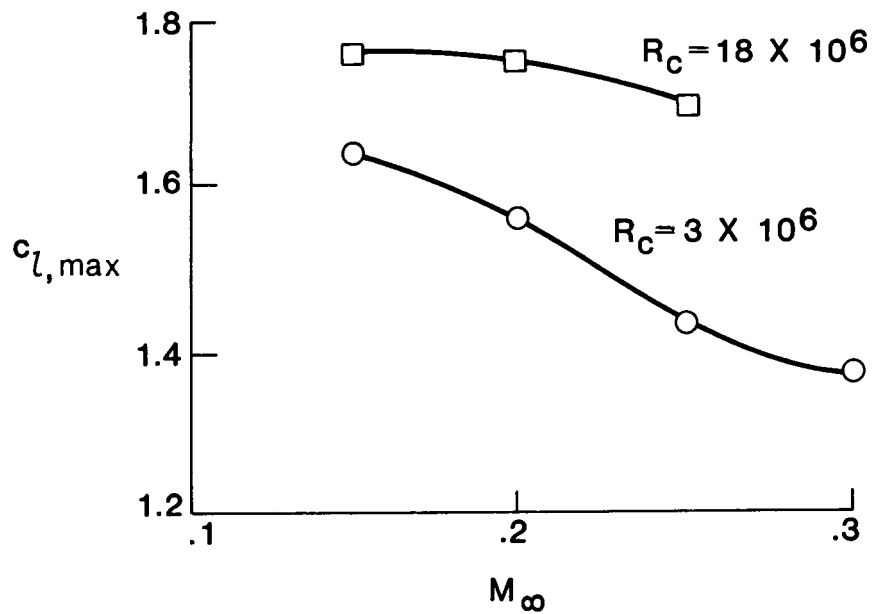
(b) Maximum lift coefficient versus Mach number.

Figure 26.- Effect of Mach number on lift performance of large-vane cruise airfoil.
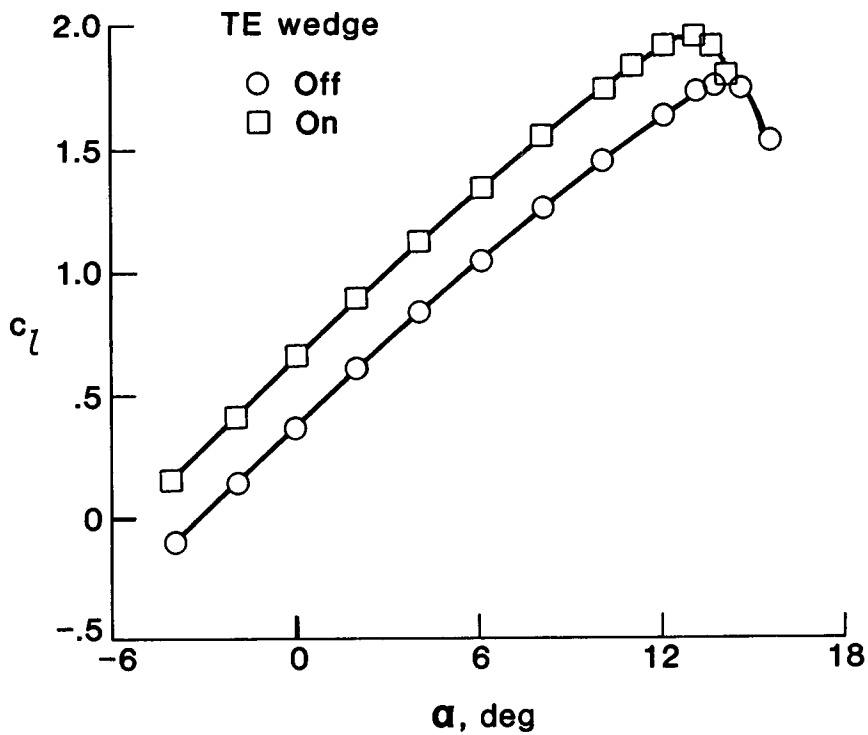
(a) Lift coefficient versus angle of attack. $R_c = 9 \times 10^6$.
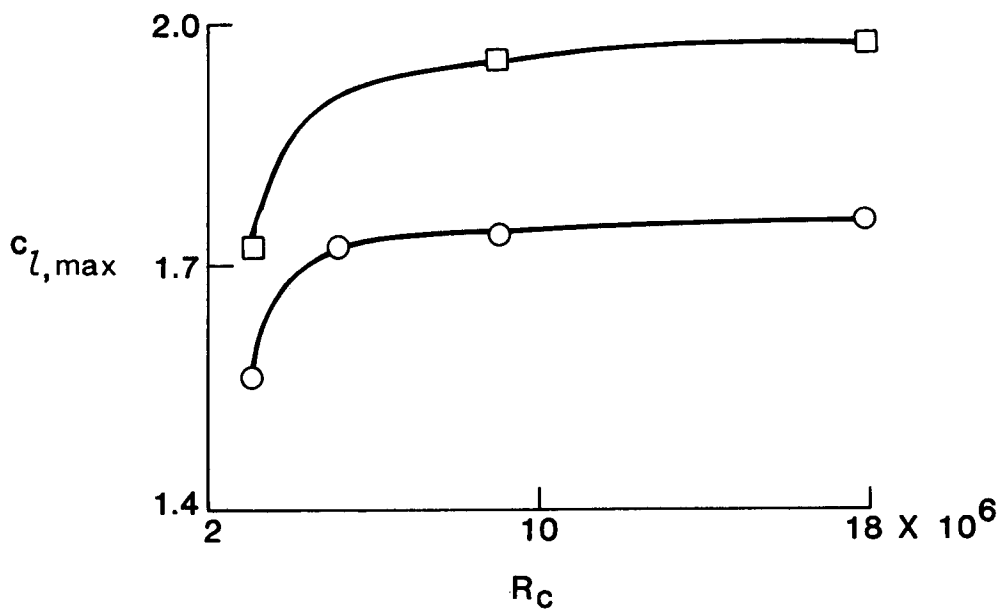
(b) Maximum lift coefficient versus Reynolds number.

Figure 27.- Effect of TE wedge on lift performance of large-vane cruise airfoil. $M_\infty = 0.2$.
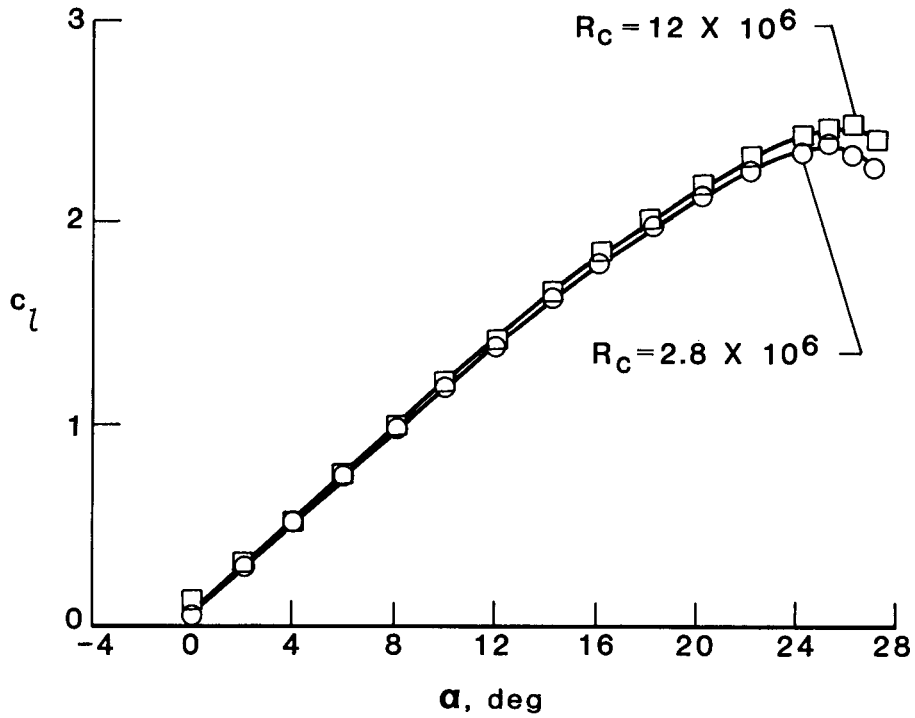
(a) Lift coefficient versus angle of attack.
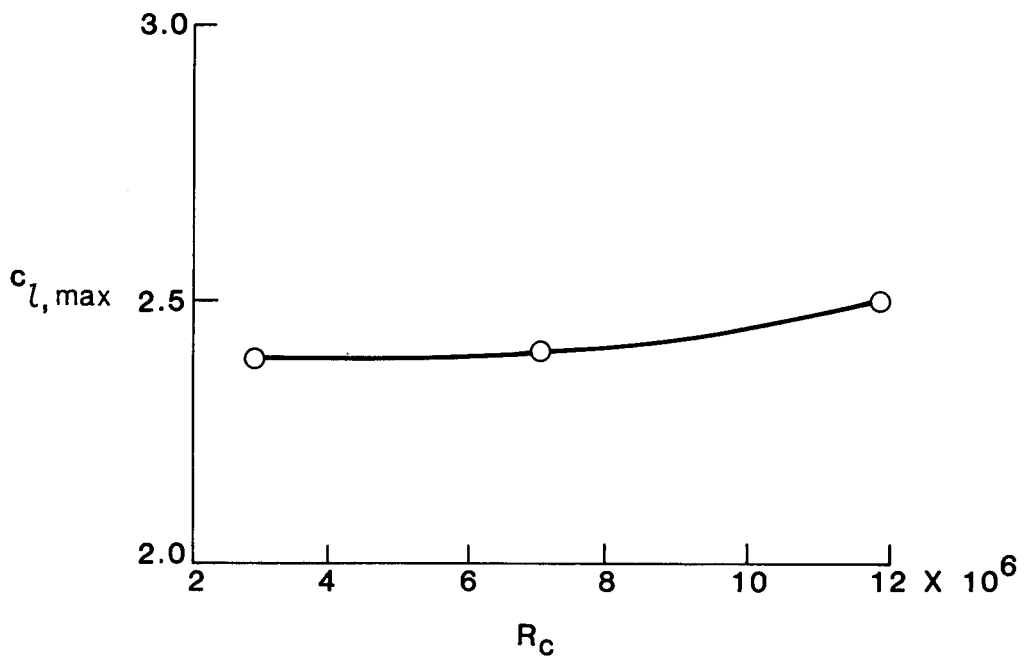
(b) Maximum lift coefficient versus Reynolds number.

Figure 28.- Effect of Reynolds number on lift performance of small-vane cruise configuration with baseline slat deflected. $\delta_S = -21°$; $M_\infty = 0.2$.
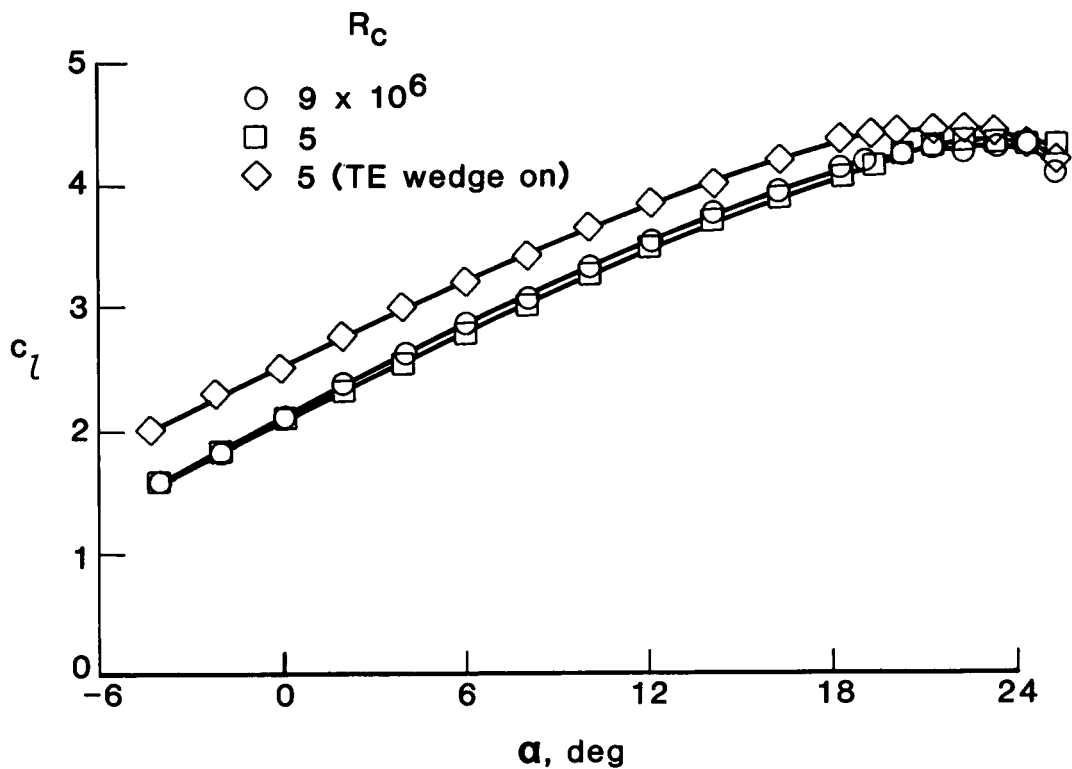
(a) Lift coefficient versus angle of attack. $\delta_f = 30°$.
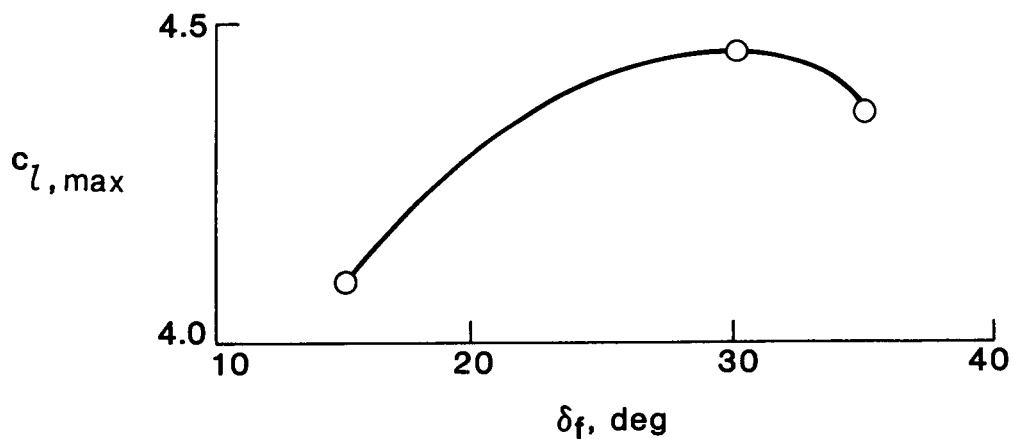
(b) Maximum lift coefficient versus flap deflection. $R_c = 5 \times 10^6$.

Figure 29.- Effect of flap deflection and TE wedge on lift performance of large-vane configuration with slat and single-slotted flap. $M_\infty = 0.2$; $\delta_s = -30°$.
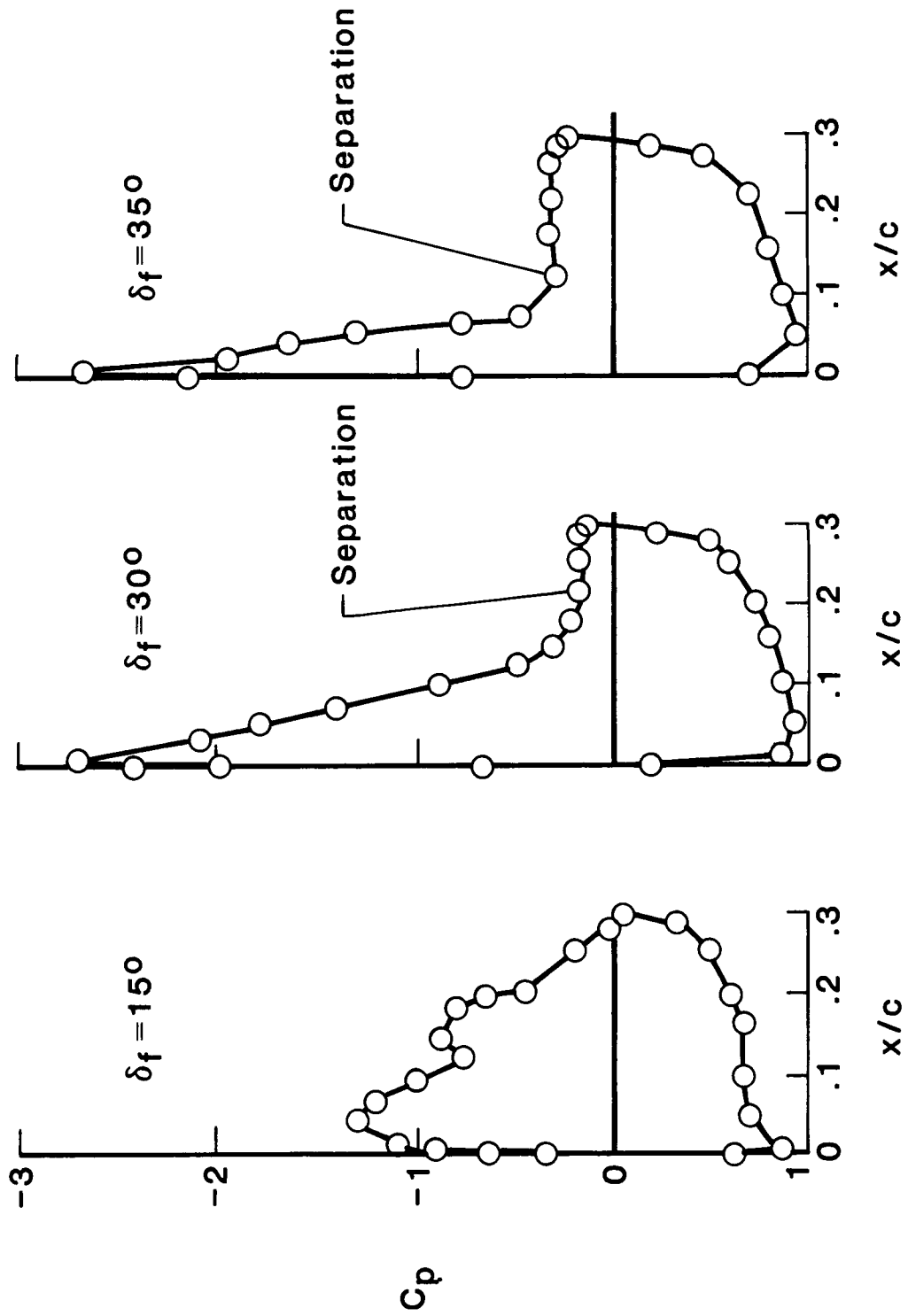
Figure 30.- Flap pressure distributions for large-vane configuration with slat and single-slotted flap. $R_c = 5 \times 10^6$; $M_\infty = 0.2$; $\delta_s = -30°$; $\alpha = 10°$.
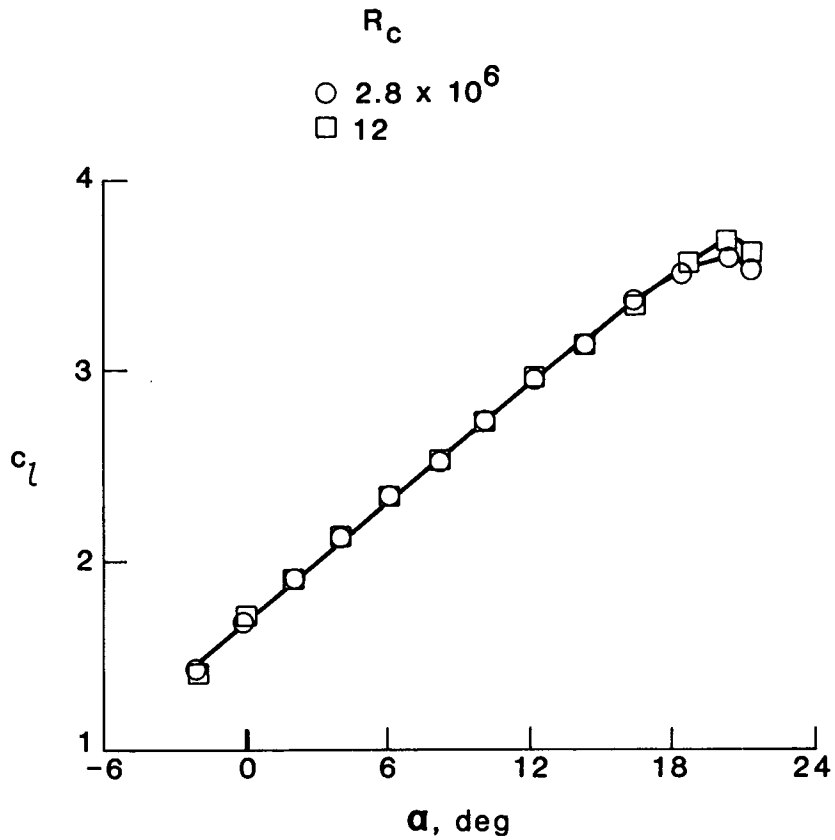
(a) Lift coefficient versus angle of attack. $\delta_f = 40°$.
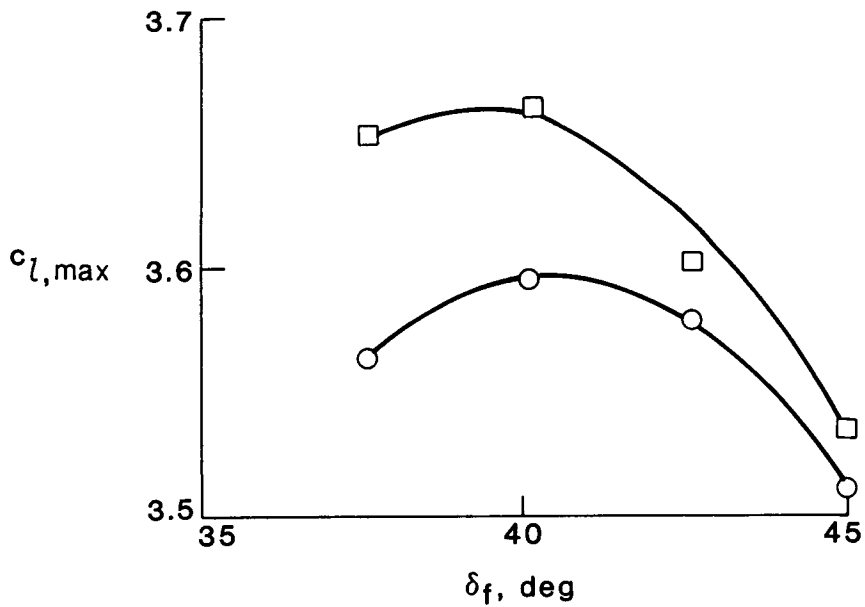
(b) Maximum lift coefficient versus flap deflection.

Figure 31.- Effect of Reynolds number and flap deflection on lift performance of small-vane configuration with baseline slat and single-slotted flap. $M_\infty = 0.2$; $\delta_s = -24°$.
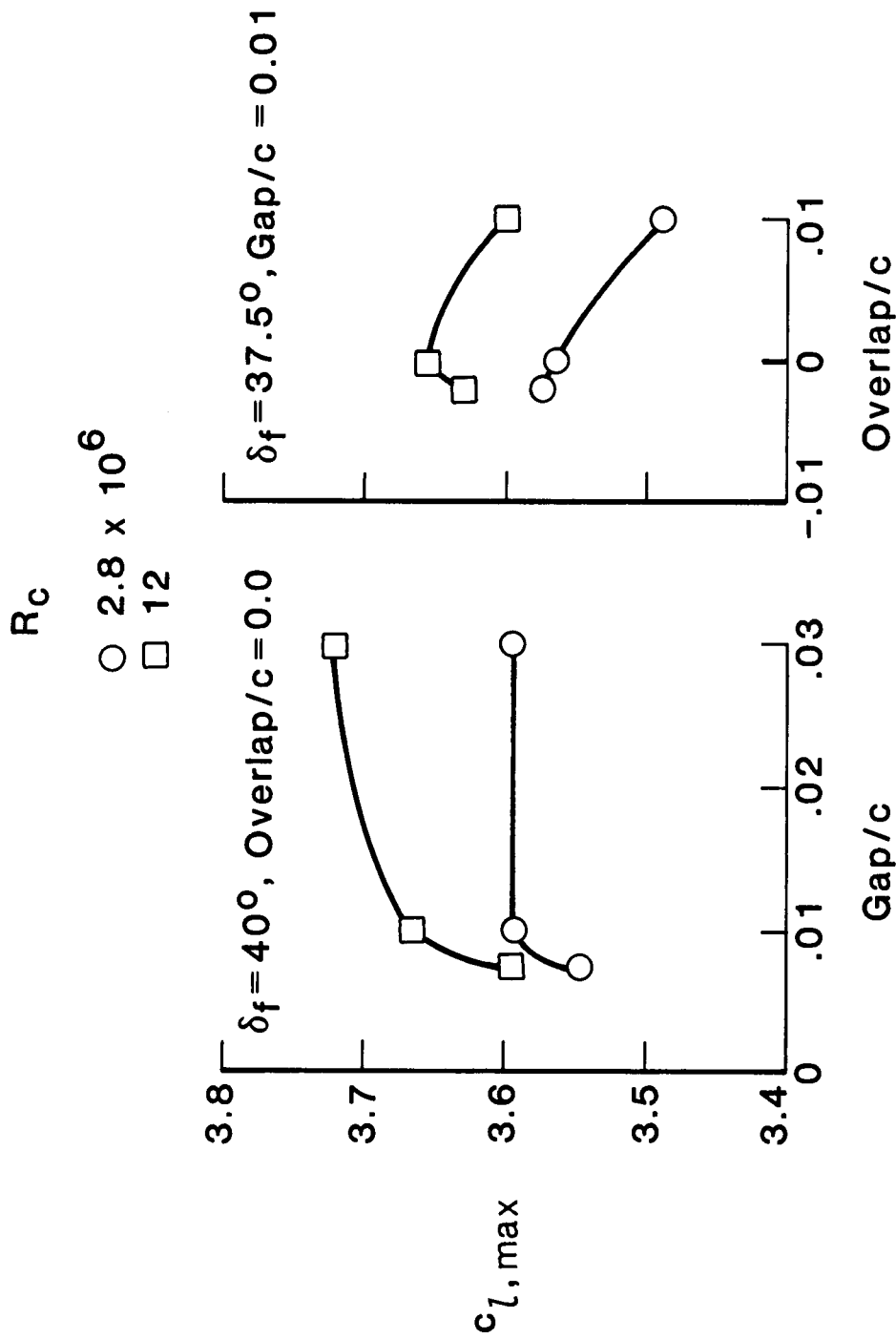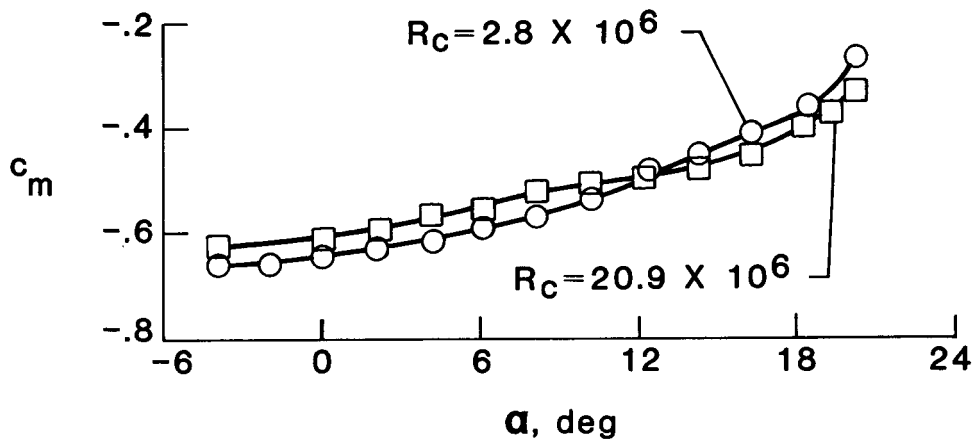
Figure 32.- Effect of Reynolds number on flap position optimization of small-vane configuration with baseline slat and single-slotted flap. $M_\infty = 0.2$; $\delta_s = -24°$.
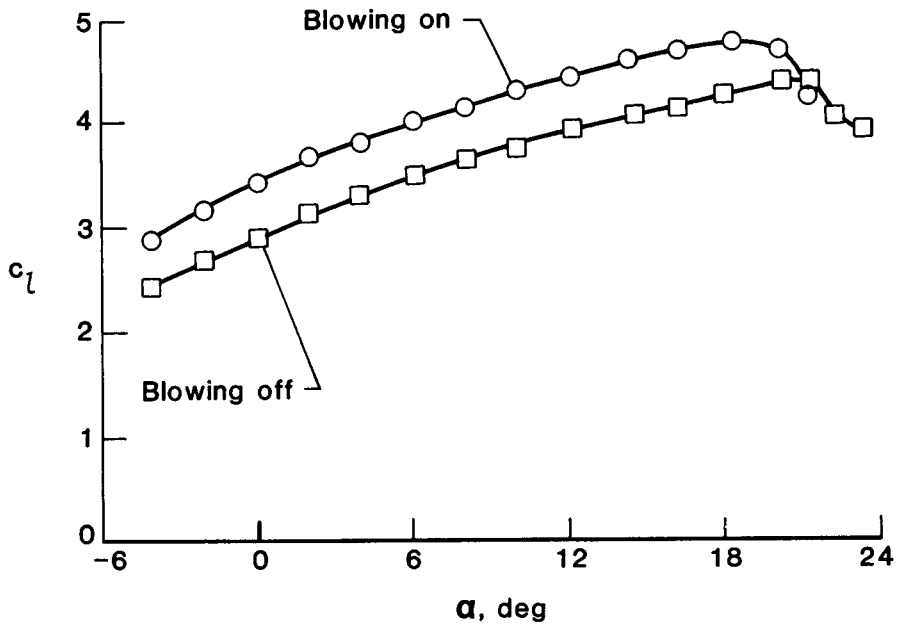
(a) Lift coefficient versus angle of attack with and
without sidewall BLC. $R_C = 3 \times 10^6$.
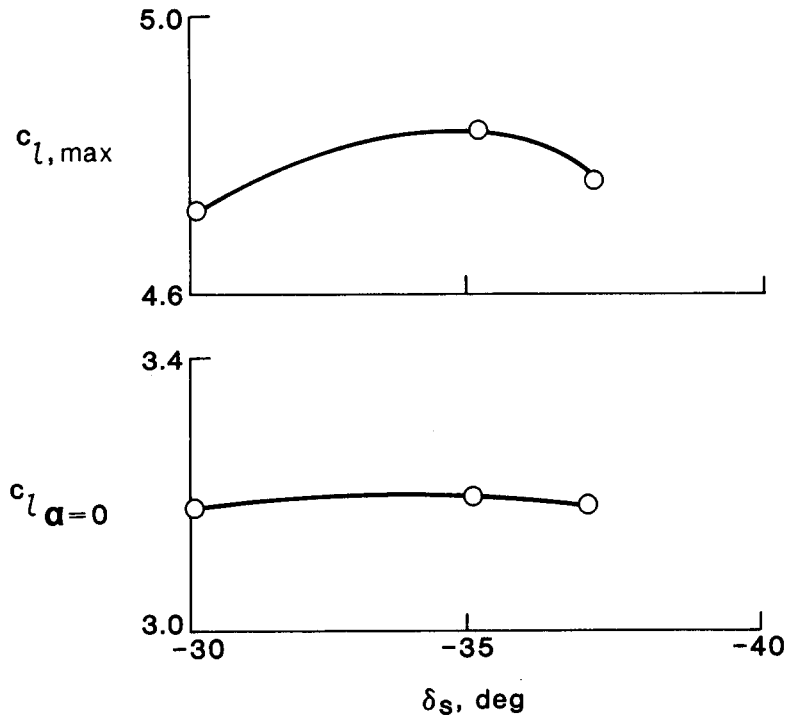
(b) Maximum lift coefficient and lift coefficient at $\dot{\alpha} = 0°$
versus slat deflection. $R_C = 9 \times 10^6$.

Figure 33.- Effect of sidewall BLC and slat deflection on lift performance
of large-vane configuration with slat and double-slotted flap.
$M_\infty = 0.2$; $\delta_S = -30°$; $\delta_V = 35°$; $\delta_f = 50°$.
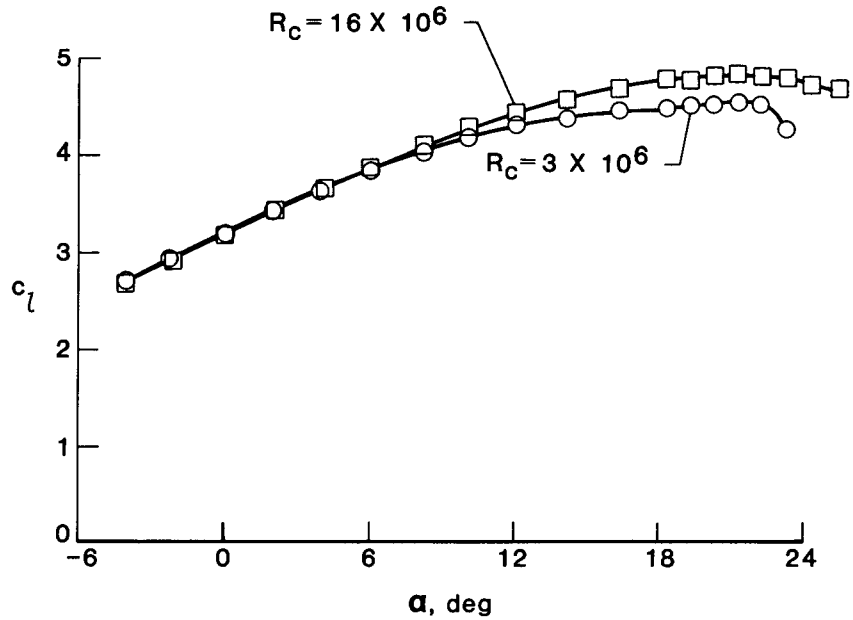
(a) Lift coefficient versus angle of attack with TE wedge off.
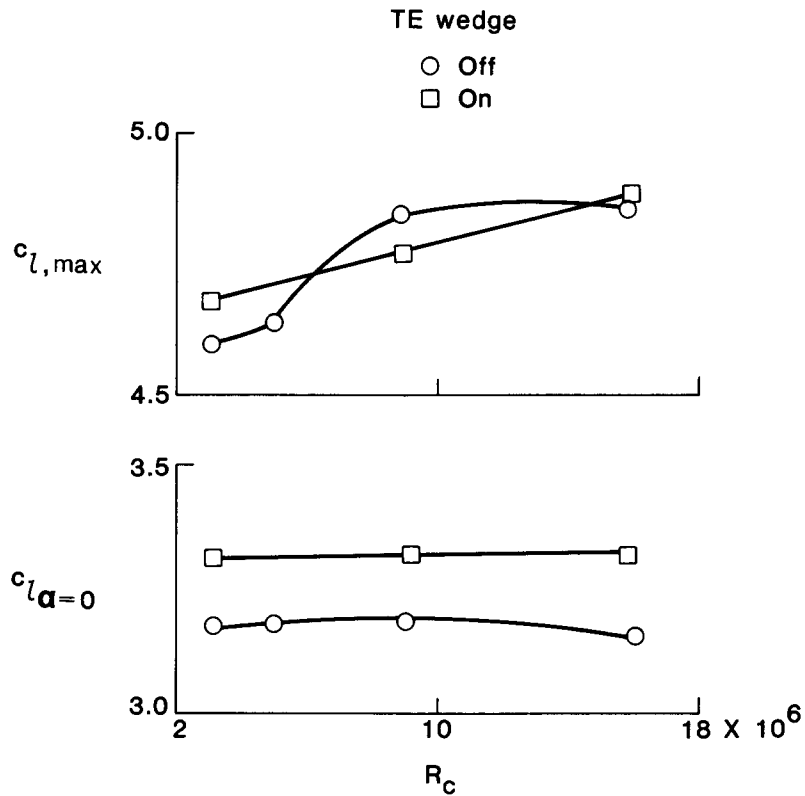
(b) Maximum lift coefficient and lift coefficient at $\alpha = 0°$ versus Reynolds number with TE wedge on and off.

Figure 34.- Effect of Reynolds number on lift performance of large-vane configuration with slat deflected -35° and double-slotted flap and with TE wedge on and off. $M_\infty = 0.2$; $\delta_V = 35°$; $\delta_f = 50°$.
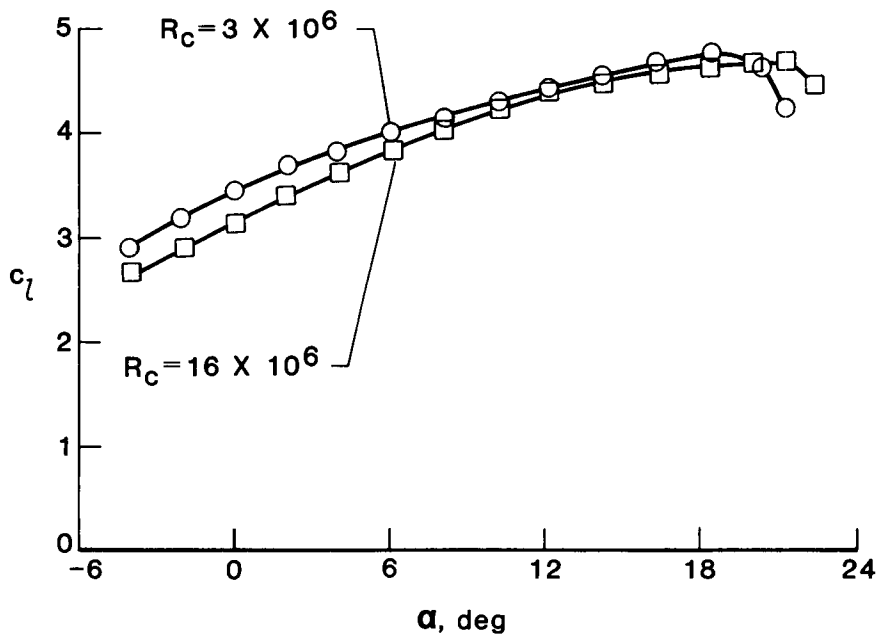
(a) Lift coefficient versus angle of attack.
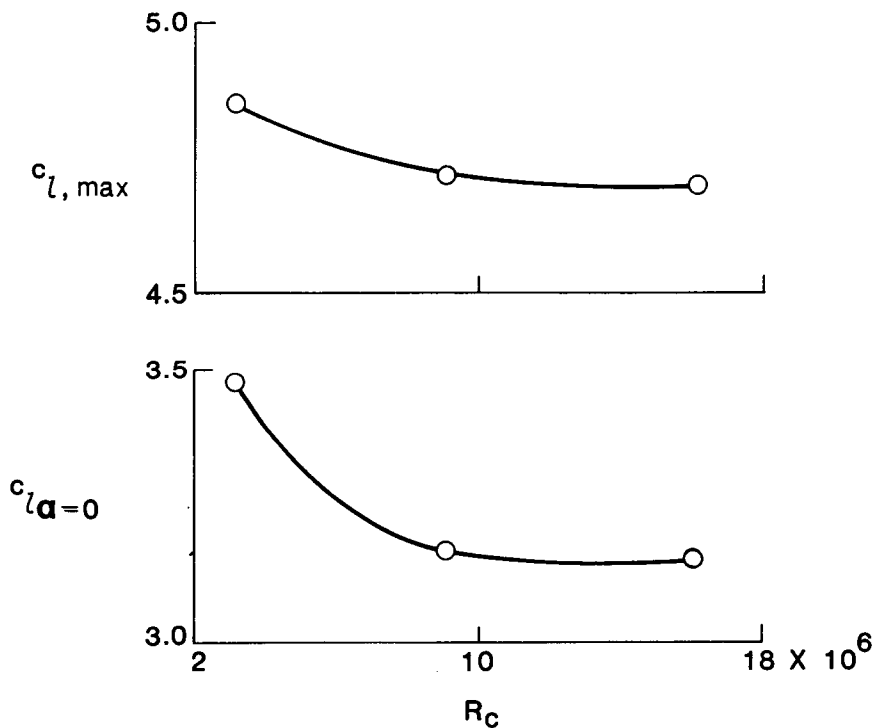
(b) Maximum lift coefficient and lift coefficient at
$\alpha = 0°$ versus Reynolds number.

Figure 35.- Effect of Reynolds number on lift performance of large-vane
configuration with slat deflected -30° and double-slotted flap.
$M_\infty = 0.2$; $\delta_v = 35°$; $\delta_f = 50°$.
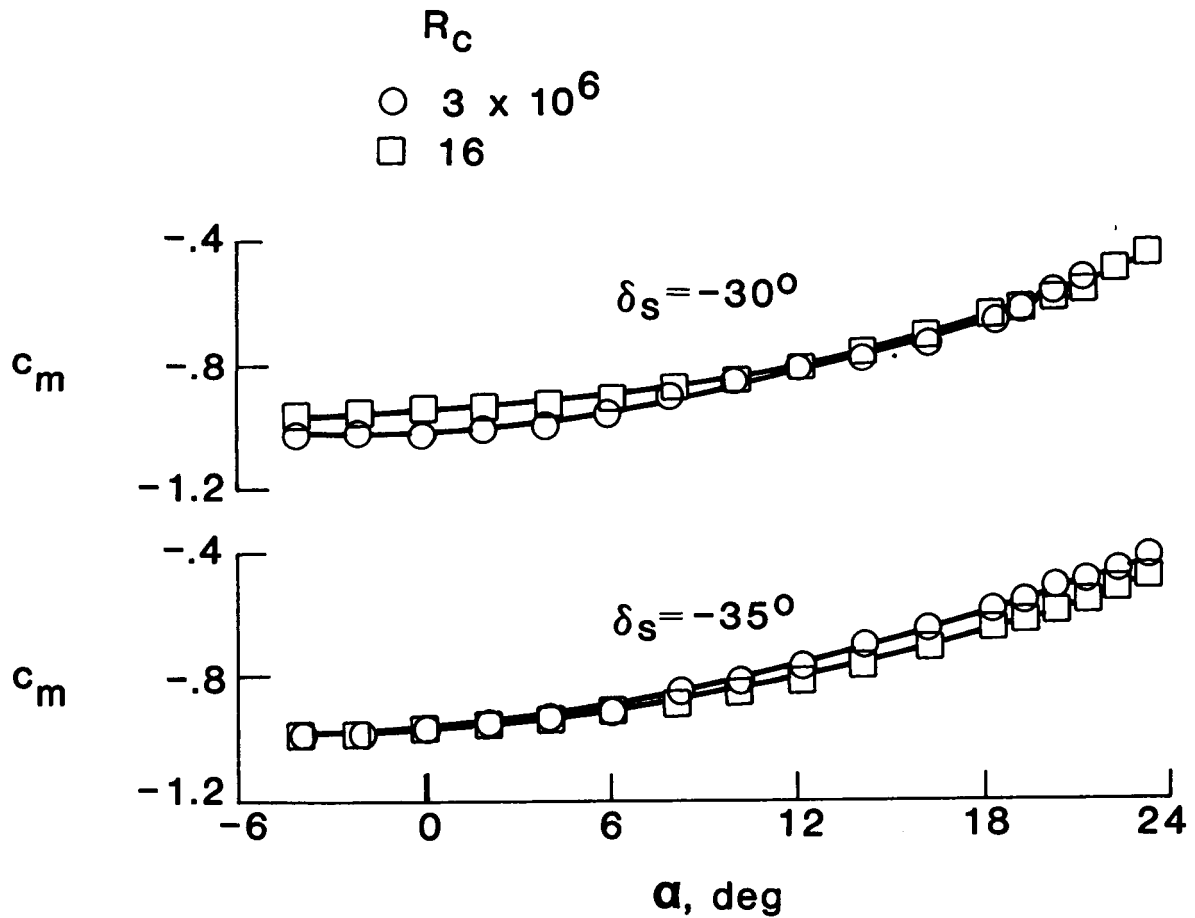
Figure 36.- Effect of Reynolds number on pitching-moment performance of large-vane configuration with slat and double-slotted flap. $M_\infty = 0.2$; $\delta_v = 35°$; $\delta_f = 50°$.
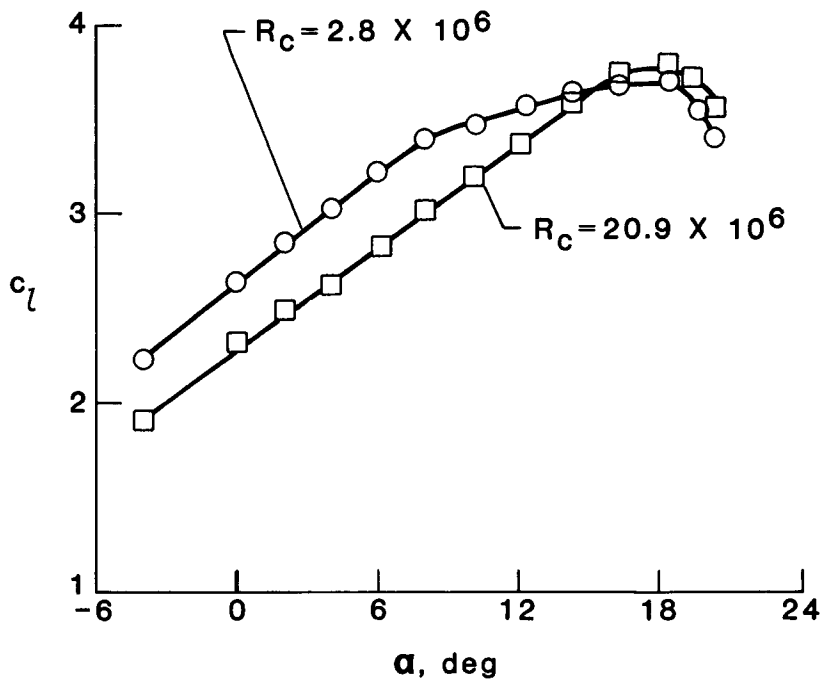
(a) Lift coefficient versus angle of attack.
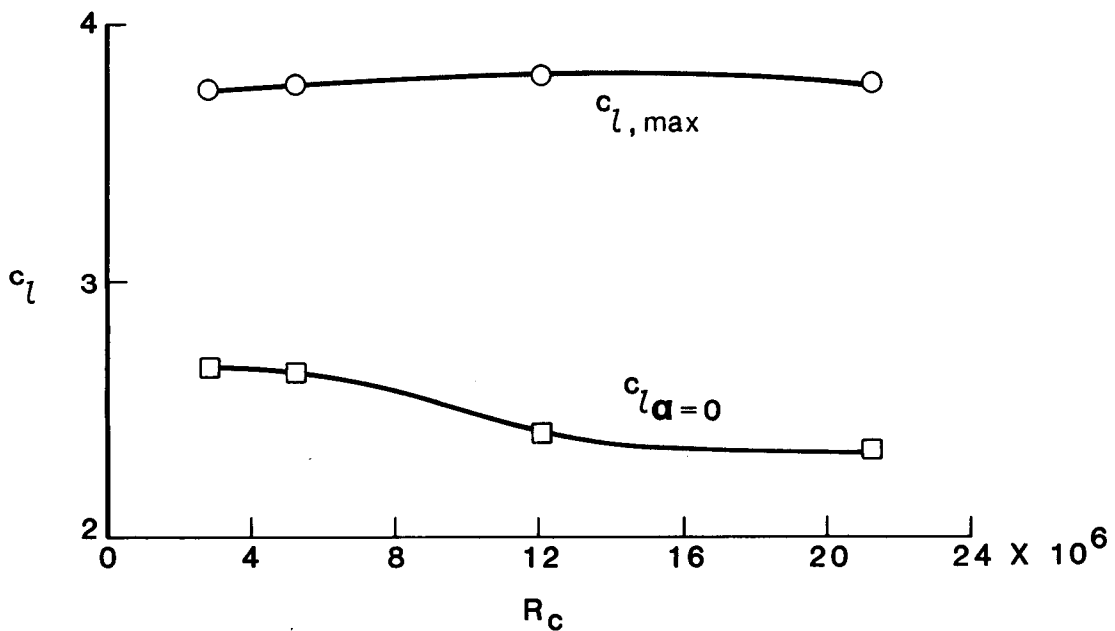
(b) Maximum lift coefficient and lift coefficient at
$\alpha = 0°$ versus Reynolds number.

Figure 37.- Effect of Reynolds number on lift performance of small-vane configuration with baseline slat and double-slotted flap. $M_{\infty} = 0.2$; $\delta_s = -24°$; $\delta_{vf} = 45°$.

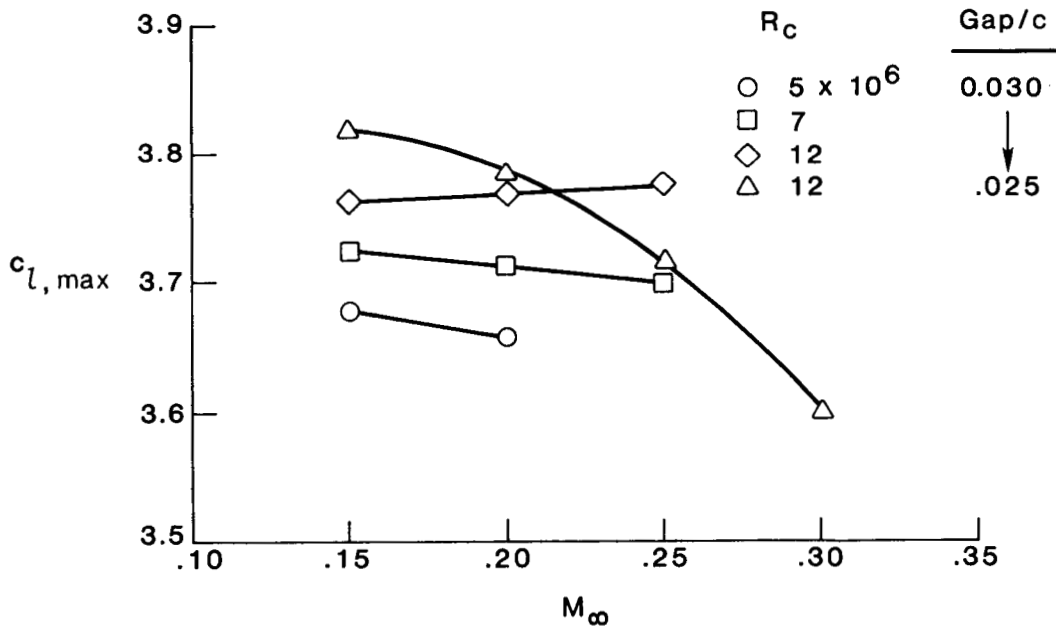Figure 38.- Effect of Reynolds number on pitching-moment performance of small-vane configuration with baseline slat and double-slotted flap. $M_\infty = 0.2$; $\delta_s = -24°$; $\delta_{vf} = 45°$.
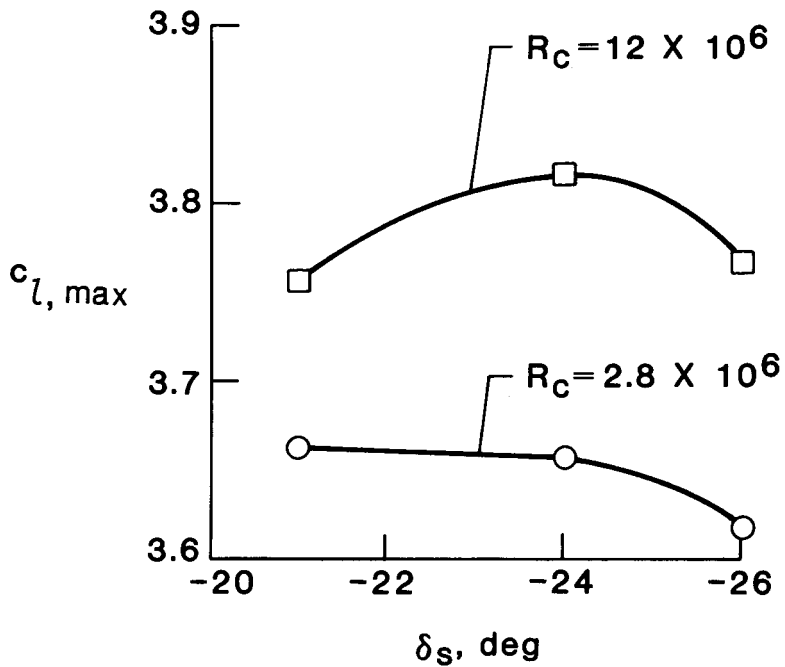

Figure 39.- Effect of slat deflection on maximum lift coefficient of small-vane configuration with baseline slat and double-slotted flap. $M_\infty = 0.2$; $\delta_{vf} = 45°$; Gap/c = 0.03; Overlap/c = 0.0.
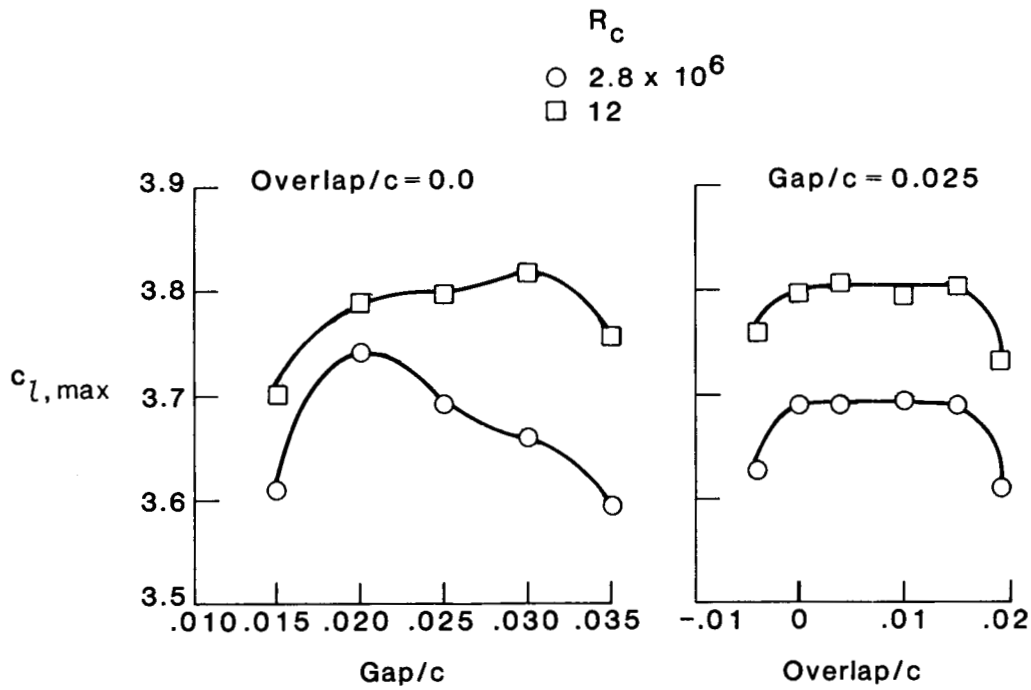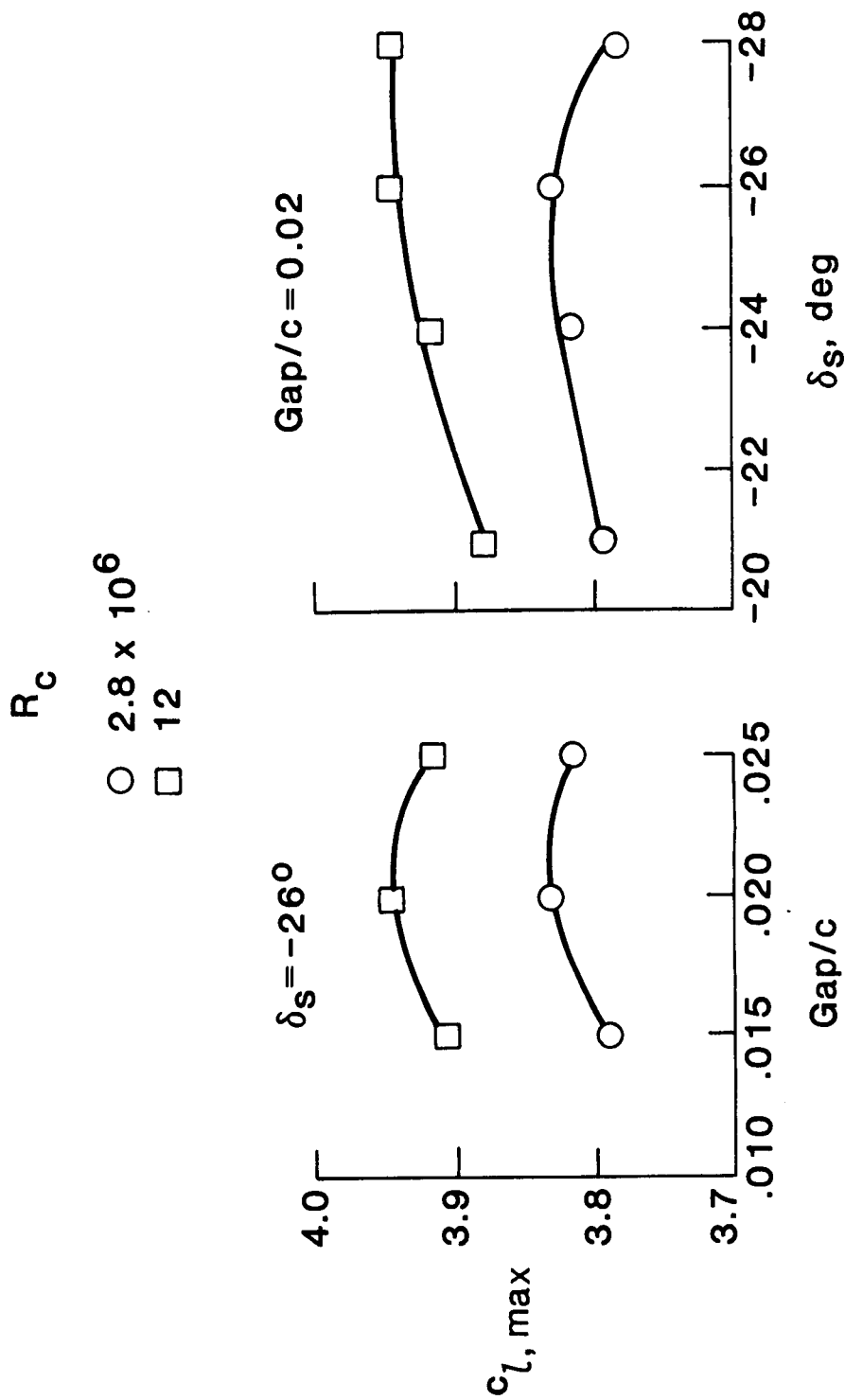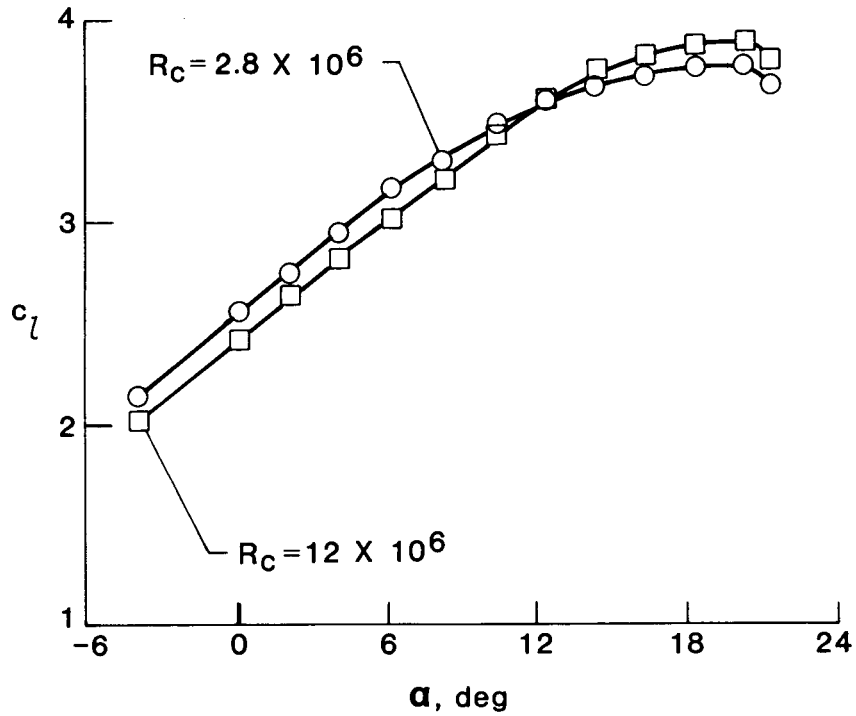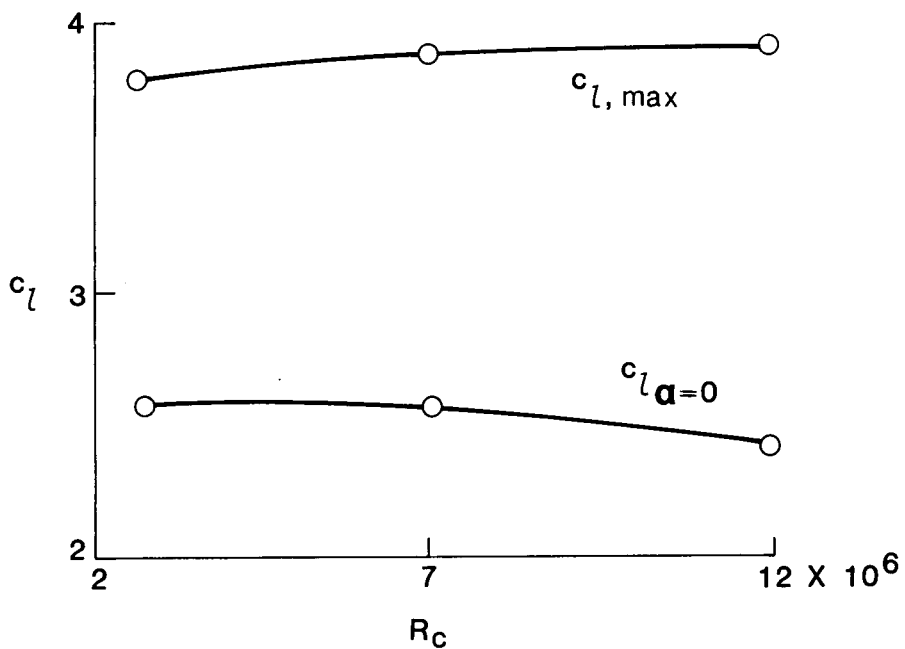
Figure 40.- Effect of Reynolds number on slat position optimization of small-vane configuration with baseline slat and double-slotted flap. $M_\infty = 0.2$; $\delta_s = -24°$; $\delta_{vf} = 45°$.

Figure 41.- Effect of Mach number on maximum lift coefficient of small-vane configuration with baseline slat and double-slotted flap. $\delta_s = -24°$; $\delta_{vf} = 45°$.
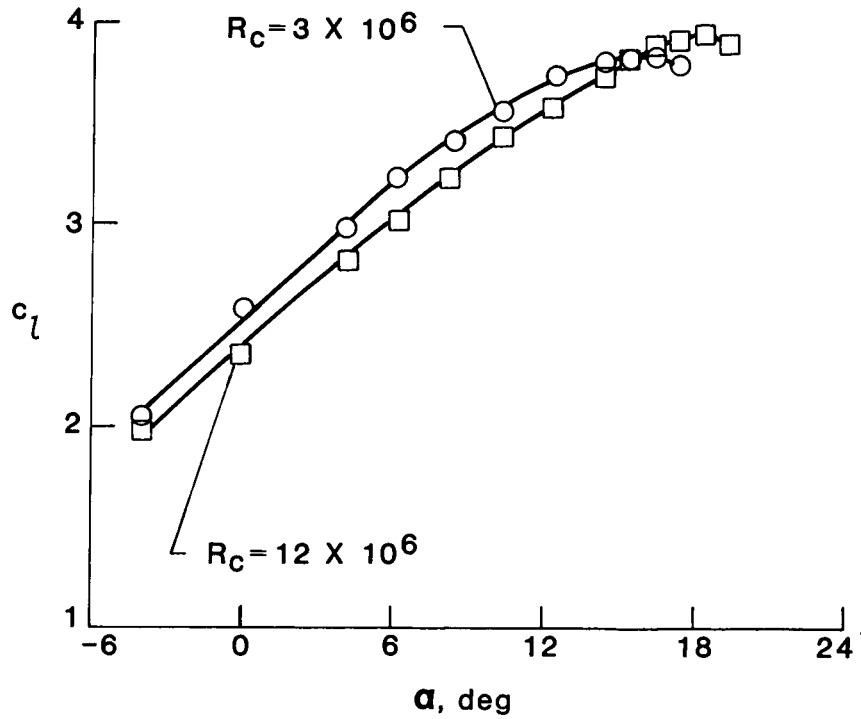
(a) Lift coefficient versus angle of attack.
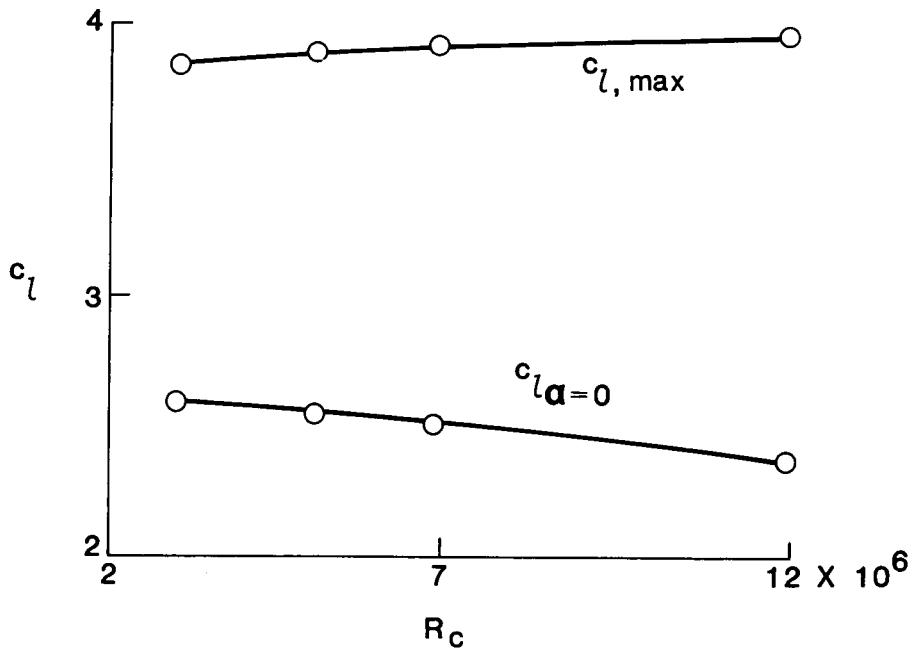
(b) Maximum lift coefficient and lift coefficient at
$\alpha = 0°$ versus Reynolds number.

Figure 42.- Effect of Reynolds number on lift performance of small-vane configuration with large-chord slat and double-slotted flap. $M_\infty = 0.2$; $\delta_s = -26°$; $\delta_{vf} = 45°$.

Figure 43.- Effect of Reynolds number on slat position optimization of small-vane configuration with large-chord slat and double-slotted flap. $M_\infty = 0.2$; $\delta_{vf} = 45°$.

(a) Lift versus angle of attack.

(b) Maximum lift and lift at angle of attack of 0°
versus Reynolds number.

Figure 44.- Effect of Reynolds number on lift performance of small-vane
configuration with large-radius slat and double-slotted flap.
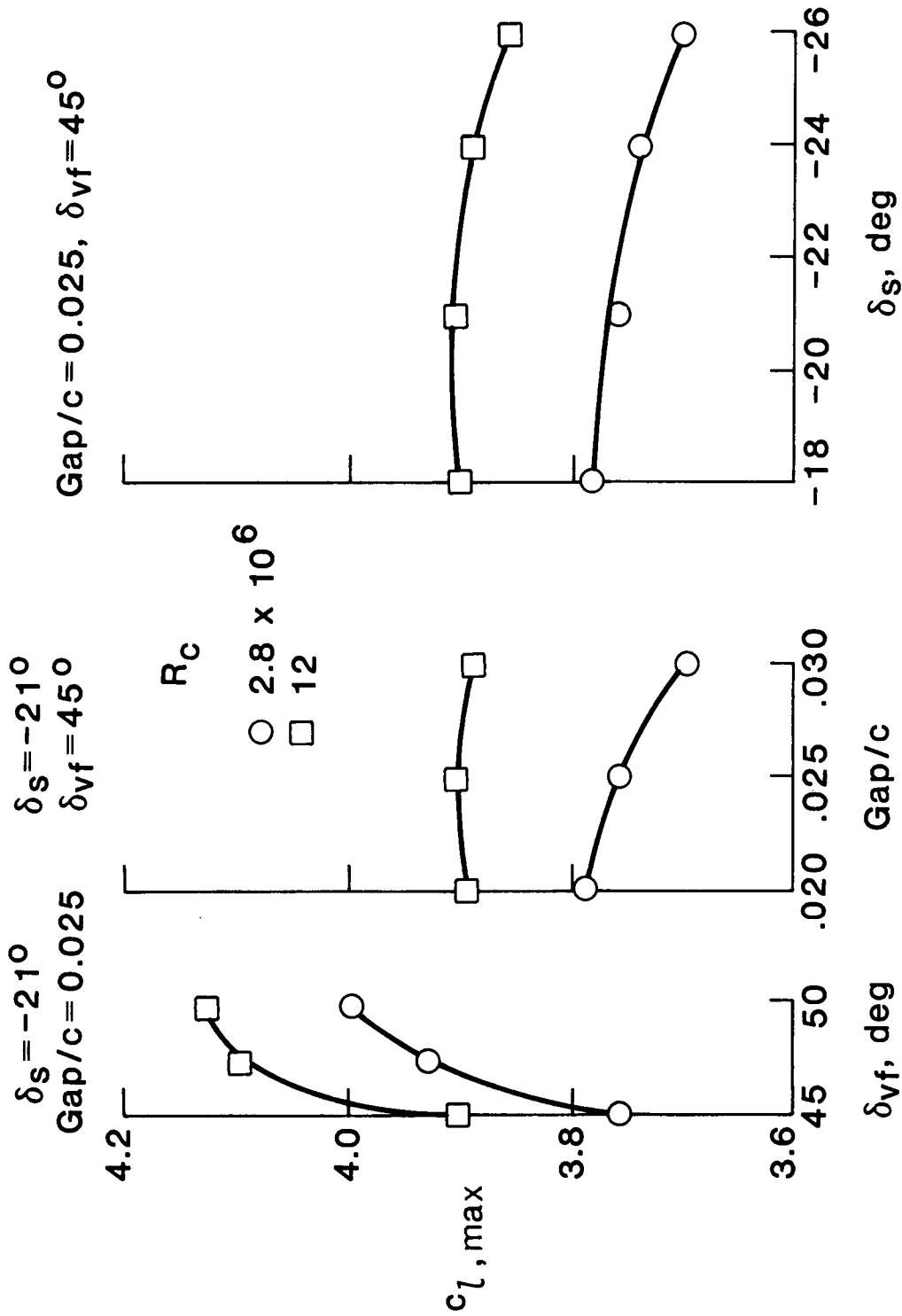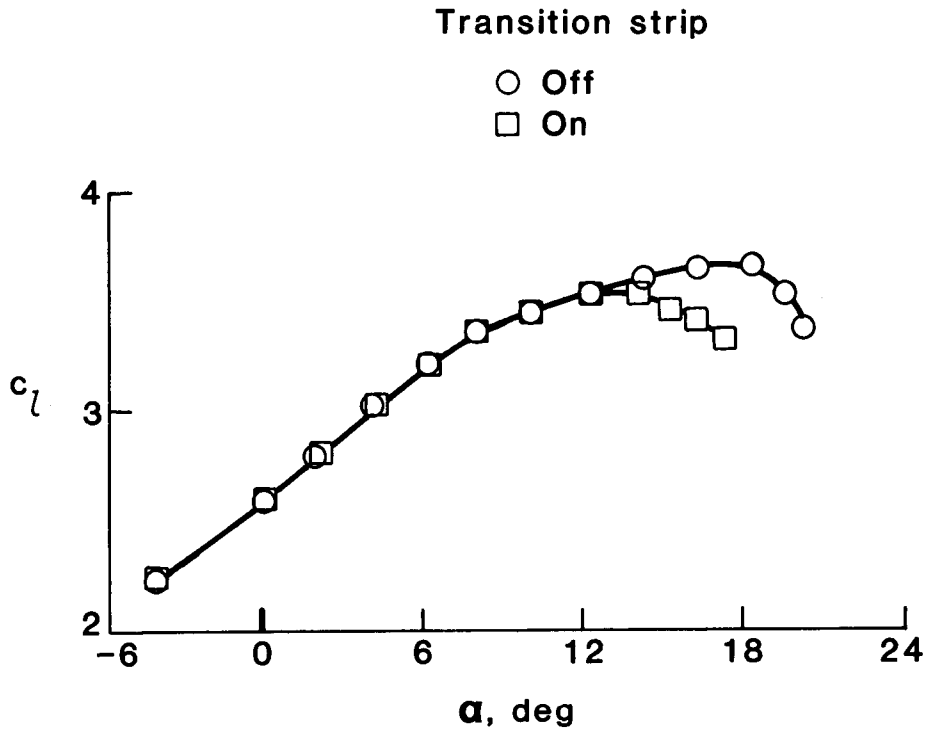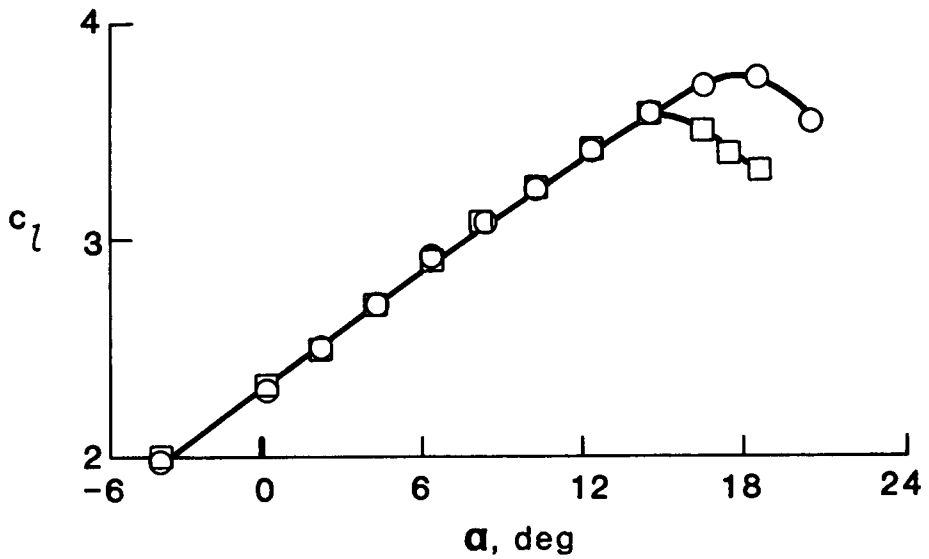$M_\infty = 0.2$; $\delta_s = -21°$; $\delta_{vf} = 45°$.

Figure 45.- Effect of Reynolds number on leading-edge-slat gap and deflection and on trailing-edge-flap deflection of small-vane configuration with large-radius slat and double-slotted flap. $M_\infty = 0.2$.

Transition strip

○ Off
□ On

(a) $R_c = 2.8 \times 10^6$.

(b) $R_c = 12 \times 10^6$.

Figure 46.- Effect of slat leading-edge transition strip on lift performance of small-vane configuration with baseline slat and double-slotted flap. $M_\infty = 0.2$; $\delta_s = -24°$; $\delta_{vf} = 45°$.
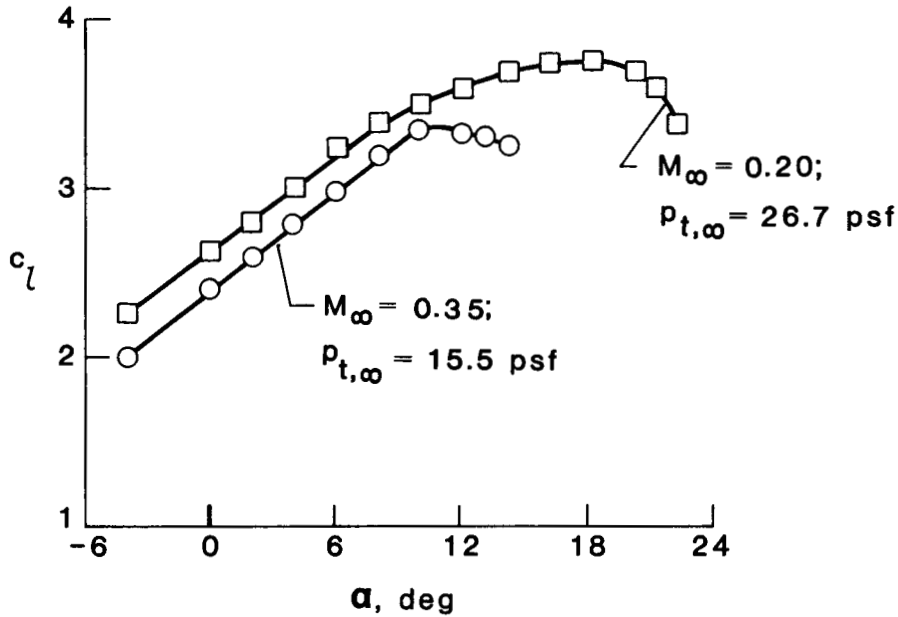
Figure 47.- Effect of varying tunnel total pressure and Mach number to maintain a constant Reynolds number for determining lift coefficient of small-vane configuration with baseline slat and double-slotted flap. $R_c = 4.9 \times 10^6$; $\delta_s = -24°$; $\delta_{vf} = 45°$.
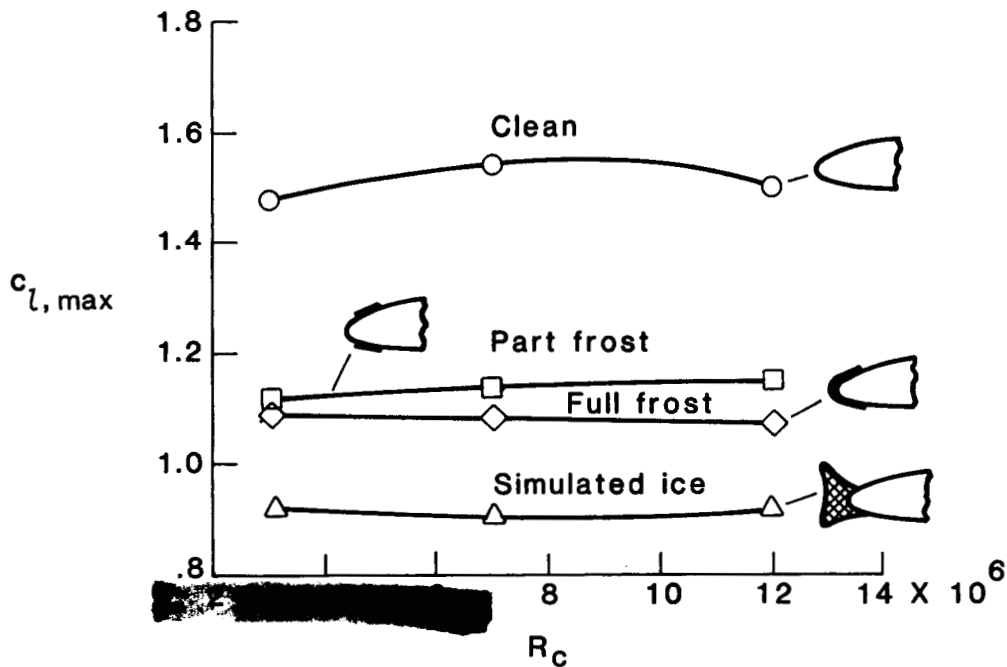

Figure 48.- Effect of Reynolds number on maximum lift performance of small-vane cruise configuration with simulated frost and ice on leading edge. $M_\infty = 0.2$.

Standard Bibliographic Page

1. Report No. NASA TM-89125	2. Government Accession No.	3. Recipient's Catalog No.
4. Title and Subtitle A Study of High-Lift Airfoils at High Reynolds Numbers in the Langley Low-Turbulence Pressure Tunnel		5. Report Date July 1987
		6. Performing Organization Code
7. Author(s) Harry L. Morgan, Jr., James C. Ferris, and Robert J. McGhee		8. Performing Organization Report No. L-16266
9. Performing Organization Name and Address NASA Langley Research Center Hampton, VA 23665-5225		10. Work Unit No. 505-60-21-01
		11. Contract or Grant No.
12. Sponsoring Agency Name and Address National Aeronautics and Space Administration Washington, DC 20546-0001		13. Type of Report and Period Covered Technical Memorandum
		14. Sponsoring Agency Code

15. Supplementary Notes

16. Abstract

An experimental study has been conducted in the Langley Low-Turbulence Pressure Tunnel to determine the effects of Reynolds number and Mach number on the two-dimensional aerodynamic performance of two supercritical-type airfoils, one equipped with a conventional flap system and the other with an advanced high-lift flap system. The conventional flap system consisted of a leading-edge slat and a double-slotted, trailing-edge flap with a small-chord vane and a large-chord aft flap. The advanced flap system consisted of a leading-edge slat and a double-slotted, trailing-edge flap with a large-chord vane and a small-chord aft flap. Both models were tested with all elements nested to form the cruise airfoil and with the leading-edge slat and with a single- or double-slotted, trailing-edge flap deflected to form the high-lift airfoils. The experimental tests were conducted through a Reynolds number range from 2.8 to 20.9×10^6 and a Mach number range from 0.10 to 0.35. Lift and pitching-moment data were obtained using the tunnel force-balance and model-support system. Each model was instrumented with a chordwise row of surface static pressure taps located at the midspan position. Summaries of the test results obtained are presented and comparisons are made between the observed aerodynamic performance trends for both models. A summary is also presented of the test results showing the effect of leading-edge frost and glaze ice formation on the lift performance of one of the cruise airfoils.

17. Key Words (Suggested by Authors(s)) Two-dimensional, high-lift airfoil Reynolds number effects Mach number effects Test techniques Leading-edge frost and ice effects	18. Distribution Statement ████████████████ Subject Category 01
19. Security Classif.(of this report) Unclassified	20. Security Classif.(of this page) Unclassified	21. No. of Pages 62	22. Price